Geomorphology 289 (2017) 27–43

Contents lists available at ScienceDirect

Geomorphology

journal homepage: www.elsevier.com/locate/geomorph

Rock avalanches clusters along the northern Chile coastal scarp

G.B. Crosta [a,*], R.L. Hermanns [b,c], J. Dehls [b], S. Lari [a], S. Sepulveda [d]

[a] Dept. of Earth and Environmental Sciences, Università degli Studi di Milano Bicocca, Milano, Italy
[b] NGU, Trondheim, Norway
[c] NTNU, Department of Geology and Mineral Resources Engineering, Trondheim, Norway
[d] Departamento de Geologia, Univ de Chile, Santiago, Chile

ARTICLE INFO

Article history:
Received 7 July 2015
Received in revised form 15 November 2016
Accepted 30 November 2016
Available online 6 December 2016

Keywords:
Rock avalanches
Dating
Modeling
Runout
Coastal scarp
Sediment yield
Erosion rate

ABSTRACT

Rock avalanche clusters can be relevant indicators of the evolution of specific regions. They can be used to define: the type and intensity of triggering events, their recurrence and potential probability of occurrence, the progressive damage of the rock mass, the mechanisms of transport and deposition, as well as the environmental conditions at the time of occurrence. This paper tackles these subjects by analyzing two main clusters of rock avalanches (each event between 0.6 and 30 Mm^3), separated by few kilometers and located along the coastal scarp of Northern Chile, south of Iquique. It lies, hence, within a seismic area characterized by a long seismic gap that ended on April 1st, 2014 with a M_w 8.2 earthquake. The scar position, high along the coastal cliff, supports seismic triggering for these clusters. The deposits' relative positions are used to obtain the sequence of rock avalanching events for each cluster. The progressive decrease of volume in the sequence of rock avalanches forming each cluster fits well the theoretical models for successive slope failures. These sequences seem to agree with those derived by dating the deposits with ages spanning between 4 kyr and 60 kyr. An average uplift rate of 0.2 mm/yr in the last 40 kyr is estimated for the coastal plain giving a further constraint to the rock avalanche deposition considering the absence of reworking of the deposits. Volume estimates and datings allow the estimation of an erosion rate contribution of about 0.098–0.112 mm km^{-2} yr^{-1} which is well comparable to values presented in the literature for earthquake induced landslides. We have carried out numerical modeling in order to analyze the mobility of the rock avalanches and examine the environmental conditions that controlled the runout. In doing so, we have considered the sequence of individual rock avalanches within the specific clusters, thus including in the models the confining effect caused by the presence of previous deposits. Bingham rheology was the most successful at explaining both the distance and the geometry of the observed events.

1. Introduction

Earthquakes have long been discussed as an important trigger for large rock slope failures (Montandon, 1933; Abele, 1974; Eisbacher and Clague, 1984; Keefer, 1984a, b; Meunier et al., 2007) and specific events have been described in detail (Shreve, 1966; Plafker and Ericksen, 1978; Adams, 1981; Jibson et al., 2006; Jibson, 2009; Owen et al., 2008; Dai et al., 2011). Large rockfalls and rock avalanches are phenomena frequently observed during earthquakes, with past and recent examples reported for major events worldwide (1911 Usoi rock avalanche, M7.4 Sarez earthquake, Pamirs, Ischuk, 2011; M7.7, Ambraseys and Bilham, 2012; 1949 Khait rock avalanche, M7.5 earthquake, Tien Shan, Evans et al. 2009a; 1959 Madison Canyon landslide, Hebgen Lake earthquake, Montana, USA, Hadley, 1964; 1964 Alaskan rock avalanches, M9.2 Anchorage earthquake, USA, Post, 1967; 1970 Huascaran ice-rock avalanche, M8.0 Ancash earthquake, Peru, Plafker and Ericksen, 1978, Evans et al. 2009b; 1999 M7.6 Chi-Chi earthquake, Tsao-Ling landslide Taiwan; M7.7 and M6.7 El Salvador earthquake, 2001, Las Colinas and other rock avalanches; 2008 Tangjiashan and Daguangbao rock avalanches, M8.0 Wechuan earthquake, China, Wu et al., 2010; Yin et al., 2011; M7.6 Kashmir 2005 Earthquake, Hattian Bala rock avalanche, Dunning et al., 2007; 2002 Black Rapids Glacier rock avalanches, M7.9 Denali Fault earthquake, Alaska, USA, Jibson et al., 2006). The location most suitable for the earthquake induced landslides to occur is close to the ridge crests, where the susceptibility to landsliding is greatest because of topographic effects. Meunier et al. (2008) observed that clustering of earthquake induced landslides occurs at steepest topographic slopes and where greatest seismic ground accelerations are present.

Beyond the local characteristics of the site and of the landscape, a major role in landslide triggering is played by the type of earthquake and the hypocenter position with respect to the susceptible areas.

Keefer (1984a) and Rodríguez et al. (1999) summarized observations on, respectively, 40 and 36 earthquakes that triggered landslides. Most of the earthquakes that triggered large rock avalanches were

* Corresponding author.
E-mail address: giovannibattista.crosta@unimib.it (G.B. Crosta).

http://dx.doi.org/10.1016/j.geomorph.2016.11.024
0169-555X/

crustal and only four were great subduction earthquakes. This statistic agrees with evidence gathered in the recent years that shallow earthquakes in continental crust commonly trigger large rock slope failures along or near the surface of rupture (Jibson et al., 2006; Sepulveda et al., 2010; Dai et al., 2011). In contrast, subduction earthquakes only occasionally trigger large rock slope failures (Miller, 1960; Keefer, 1984b). The subduction zone along the pacific coast of South America has experienced multiple historical earthquakes. Systematic landslide mapping has been undertaken following each of these earthquakes (Chimbote earthquake M8.0, Plafker and Ericksen, 1978; Pisco earthquake M7.9 in 2007, Zavala et al., 2009; Diercksen, 2012) or semi-systematic landslide mapping (Valdivia earthquake, M9.5 in 1960, Weischet, 1960; Arequipa earthquake, M8.5 in 2001, Keefer and Moseley, 2004; Maule earthquake M8.8 in 2010). During other subduction earthquakes with magnitudes M7.7 and M8.1 (1995, 2007 the Antofagasta and the Tocopilla earthquakes, respectively) along the pacific coast of South America, landslide activity was so low that no landslides were even mapped.

Of these data sets, the most outstanding events, the Valdivia (1960) and the Maule (2010) earthquakes, are the largest and 6th largest earthquake instrumentally recorded on earth, respectively. Again, no large rock slope failures have been reported in the Andes although large clusters of rock avalanche deposits exists (Penna et al., 2011; Hermanns et al., 2011) at a distance that falls within the magnitude-distance relationship given by Keefer (1984a) for disrupted slides (e.g. rock avalanches). During the M7.9 Pisco earthquake in 2007, a ~25,000 km^2 area was affected by landslides. However, no rock avalanche was triggered although multiple prehistoric rock avalanche deposits were observed in the area and most damage to houses occurred in villages built on rock avalanche deposits (Zavala et al., 2009). The only subduction earthquake that ever was reported to have triggered a rock-avalanche in the Andes occurred in 1970 and triggered the catastrophic Nevado Huascaran rock-ice avalanche (Plafker and Ericksen, 1978) in the Cordillera Blanca of Peru. However, only 8 years earlier, a similar rock-ice avalanche happened on the same rock face, but with no obvious trigger (Plafker and Ericksen, 1978), indicating that the slope stability was greatly reduced prior to the earthquake. In contrast, the M7.3 crustal earthquake in 1946 triggered several rock avalanches close to its epicenter, just about 60 km from Cerro Huascaran (Heim, 1949; Kampherm, 2009). The large potential of crustal earthquakes triggering rock avalanches in the Andes is also highlighted by the M6.2 Aysén earthquake (2007) that triggered two rock-avalanches in a distance of <2 km (Sepulveda et al., 2010). All these seismically triggered rock slope failures had volumes of up to a few tens of millions of cubic meters. Interestingly, the only historic mega rock slope failure in the Andes, the 1974 Mayunmarca rockslide (Peru), with a volume larger 1 km^3, was not related to any seismic event (Kojan and Hutchinson, 1978; Hermanns et al., 2008).

Our study area (between latitude 20°5′S and 20°4′S) lies along the hypo arid coastal mountains of northern Chile. This area is characterized by multiple rock avalanche deposits with volumes up to several tens of million cubic meters (Yugsi Molina et al., 2012a; Mather et al., 2014). These failures occur predominantly in spatial clusters and are locally preserved due to the presence of a well-developed coastal plain. Much larger rock slope failures, with magnitudes up to several cubic kilometers, occur on the western Andean slope (Wörner et al., 2002; Strasser and Schlunegger, 2005; Pinto et al., 2008) and within most of the valleys draining the Andes towards the Pacific (Crosta et al., 2012, 2014). Only few of such large rock slope failures have been documented in the coastal cordillera, although suspicious sinuous coastlines of similar size exist that have been interpreted as landslide source areas (Crosta et al., 2012, 2014; Mather et al., 2014). The study area coincides today with the most important seismic gap in the subduction zone of the Nazca plate below the South American continent with no major earthquakes between those of 1868 and 1877 (Beck and Ruff, 1989; Lomnitz, 2004; Baker et al., 2013). This gap ended on April 1st 2014 with a Mw 8.2 earthquake, preceded a week before by multiple ~M7 earthquakes. Stress on the bordering segments had been released during the 1995 M8.1 Antofagasta earthquake, the 2001 M8.5 Arequipa earthquake, and the 2007 M7.7 Tocopilla earthquake. Mather et al. (2014) suggest that rock slope failures in this segment may represent paleoseismical records for the long term seismic gap.

We present the results of an extensive study in a relatively small area just south of Iquique affected by three main groups of rock avalanches. The aim of the study is to assign a possible age to these rock avalanches, to understand the triggering conditions and the mechanisms of transport and deposition. In this paper, we test the following hypotheses: the volumes released by a sequence of landslide events from a source area follow a logarithmic relationship with the order of occurrence. The erosion rate resulting from the instabilities studied along the northern Chile coastal cliff agrees with previous estimates from the literature for seismic induced landslides; the main features typical of these clusters of rock avalanches suggest a seismic triggering. To these aims, different approaches have been applied including field recognition and mapping, sample collection for dating of the rock avalanche events, InSAR measurements to evaluate the state of activity along a sector of the coastal cliff, and numerical modeling of rock avalanche run-out to evaluate the required physical mechanical properties to fit the deposit geometry and characteristics.

2. Study area

The study area is located in the northern part of Chile (Tarapaca province) along the coastal zone of the Atacama desert (Fig. 1) characterized by a mean annual precipitation of about 1 mm. Here, some huge rock avalanches and rotational landslides (Crosta et al., 2012, 2014) have been mapped in an area which stretches between Iquique and Arica from the ocean up to an elevation of about 3000 m a.s.l. The Coastal Cordillera comprise basaltic andesites and granodiorites cut by N–S to NE–SW trending, and normal faults bounding a series of half-grabens (Paskoff, 1978).

The western margin of the Cordillera is a coastal scarp, a significant break in slope 600 to 1500 m high, locally ending directly into the ocean or along a coastal plain. The latter is characterized by variable width, a generally smooth topography, with few preserved terraces, and generally gently inclined towards the ocean. This is the case of the area just to the south of Iquique on which this paper is focused (Figs. 1, 2). These features required a period of constant sea level long enough to allow for the cutting of the high coastal cliff, and a successive series of uplift steps allowing for the development of marine terraces. Regard et al. (2010) studied the Pacific coast along the Central Andes, between 15°S and 30°S characterized by the presence of the coastal plain and the steep coastal cliff. They mapped in particular the cliff foot located generally at 110 m a.s.l., and dated it to about 400 kyr ± 100 kyr (within the Marine Isotopic Stage MIS11). This suggests a renewal of the uplift since then with a calculated uplift rate for the study area, south of Iquique, ranging between 0.1 and 0.2 mm/yr.

The study area, south of Iquique, is characterized by a sequence of layered sedimentary rocks. The rock avalanche scars (Figs. 2, 3) are prevalently located in sandstone and laminated rocks dipping with the slope (cataclinal, 30° to 40°) and covered at the cliff top by alluvial conglomerates characterized by polygenic angular to subangular clasts in a brownish sandy-silty matrix. Two main Jurassic formations have been affected by these rock avalanches, the Guantajaya formation and the underlying Caleta Ligate formation (Novoa, 1970). The former is mainly composed of sandstone and frequently thinly laminated siltstones, black bituminous to reddish, and with some gypsum. The latter is a marine sedimentary sequence with black siltstones and red to yellowish sandstones.

Because of the relative position of the three clusters of rock avalanches along the N–S trending coastal cliff, we will refer to them as northern, central and southern cluster (N, C and S in Fig. 1c). The central

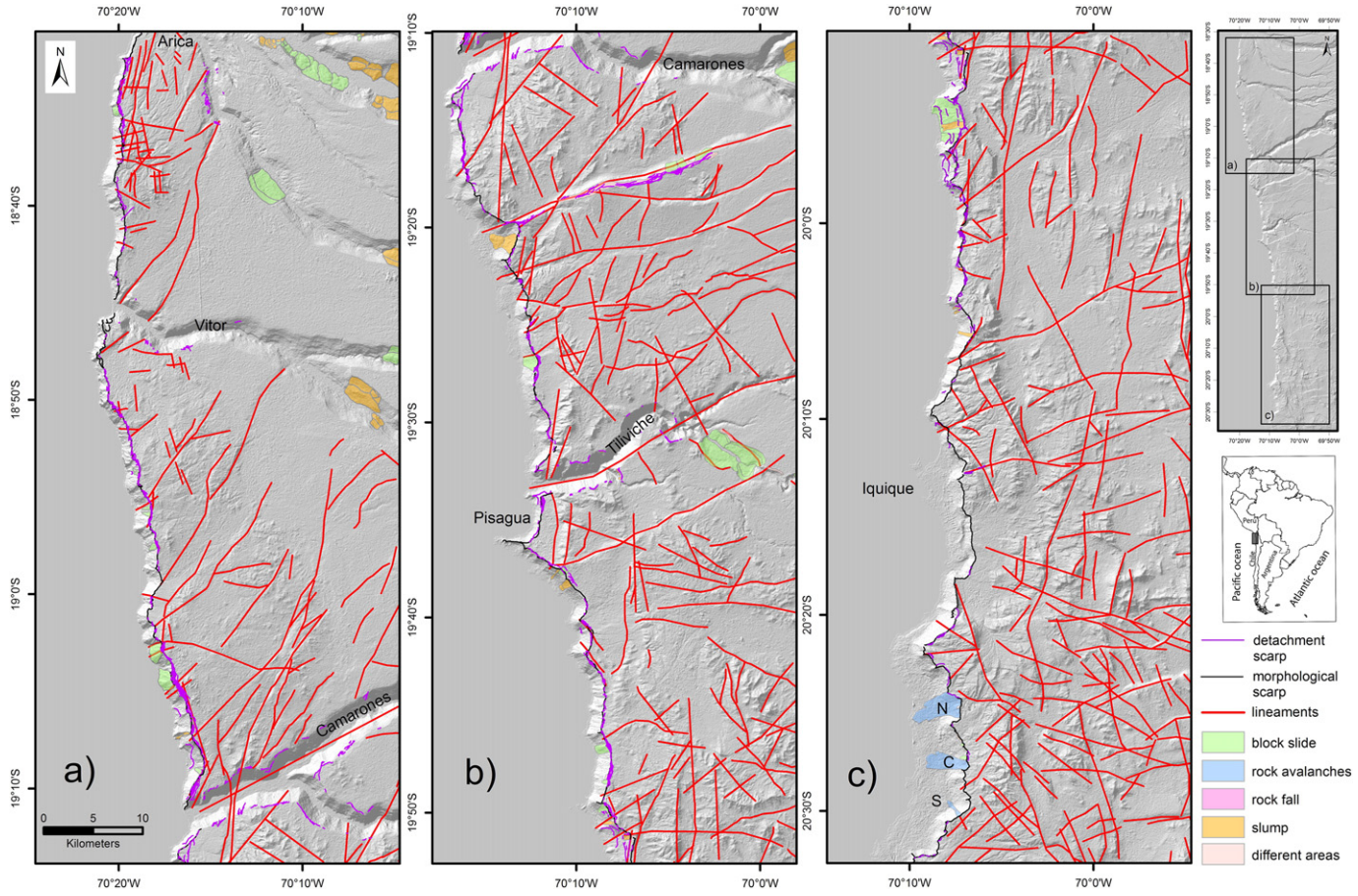

Fig. 1. Map of the main lineaments and of the main instabilities recognized along the coastal cliff between Arica to the North (a) Pisagua (b) and Iquique to the South (c). The rock avalanches studied in this paper (N, C, S) are located at the extreme southern end of the area (panel c) Some of the large landslides mapped inland and shown here are part of a larger inventory (Crosta et al., 2012, 2014) for the area.

rock avalanche deposit was already recognized and mapped by Novoa (1970) as a single major deposit, with no mention about the two other clusters neither in Novoa nor more recently by Mather et al. (2014). Both the coastal scarp and the upper sector beyond the crest are covered by abundant aeolian deposits and sand dunes which mask the rocky outcrops and locally the rock avalanche deposits.

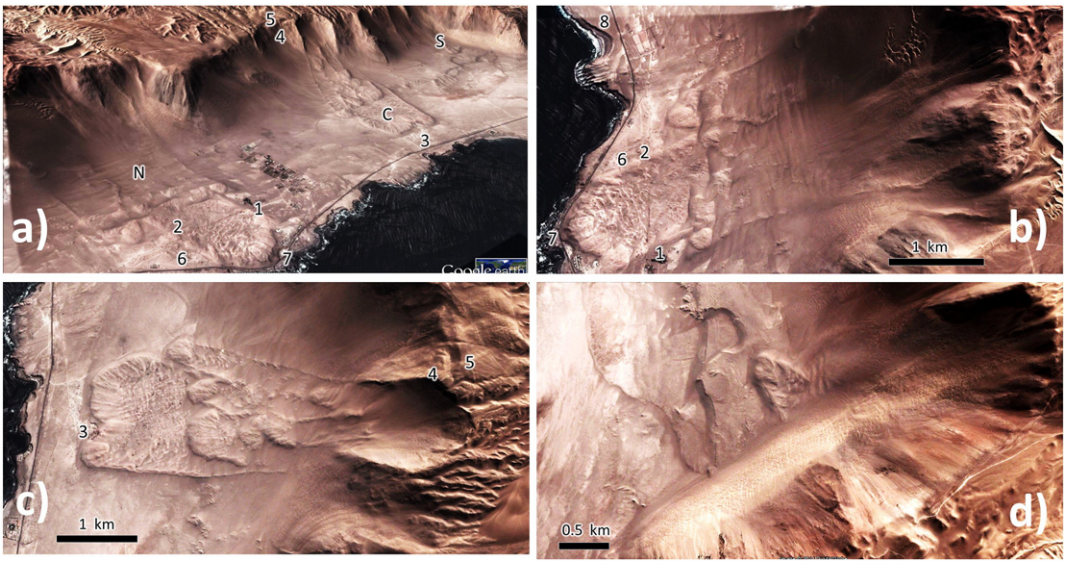

Fig. 2. a) General view of the coastal cliff and plain south of Iquique, with the three groups (N, C and S) of rock avalanches: b) Los Verdes, or northern, c) central, d) southern positioned at the farthest cliff sector with a trend roughly perpendicular to the coastline. Numbers in the figures represent: 1) and 2) position of the cross cut by the new highway with outcrops shown in Fig. 8; 3) guano quarry and cut through the main lobe of the central cluster as in Fig. 7; 4) position of the tension cracks shown in Fig. 4; 5) main scarp of the rockslide observed north of the central cluster scarp (see text for more comments). Photos courtesy from Google Earth.

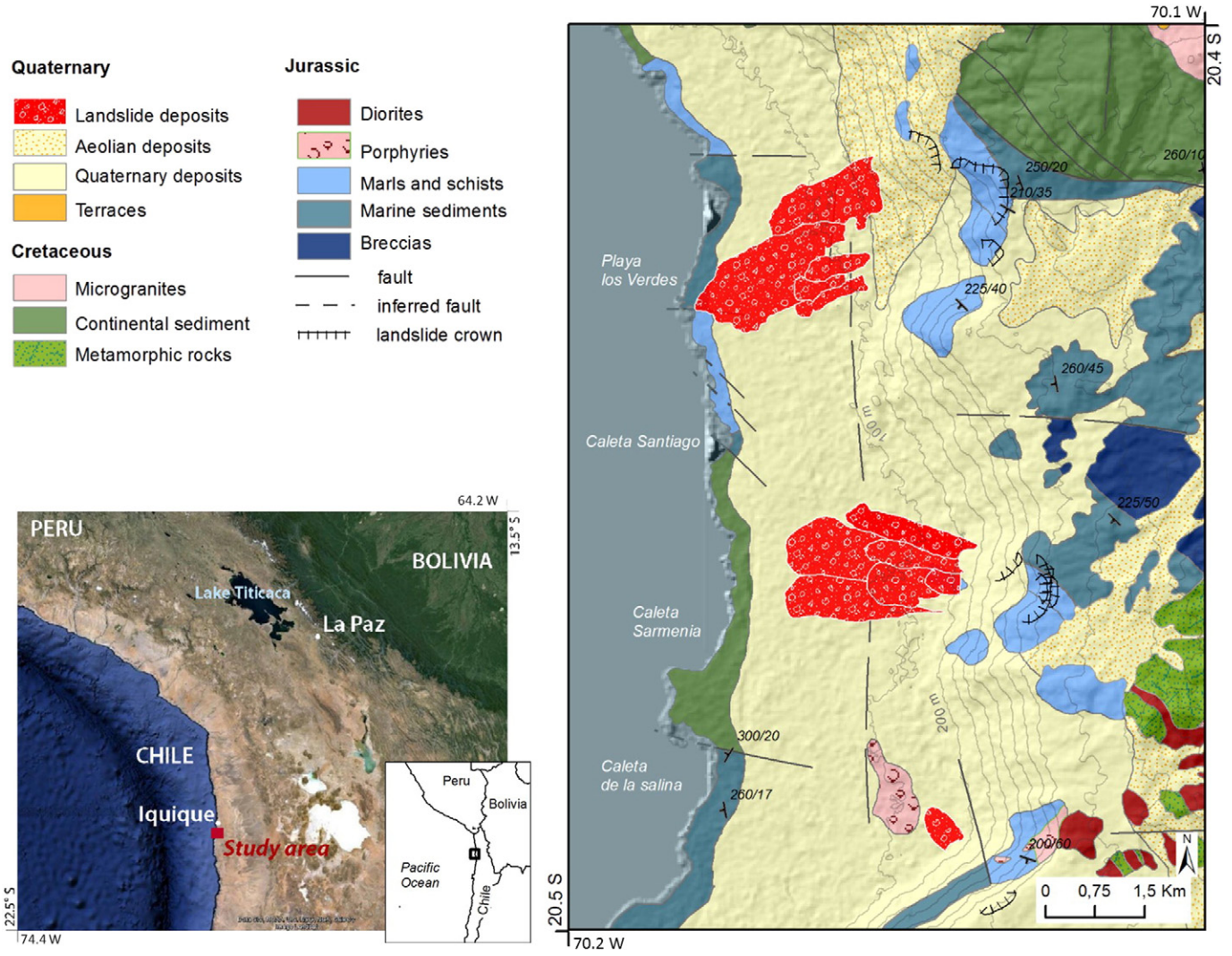

Fig. 3. Simplified geo-lithological map for the study area (after Novoa, 1970). For the general location see image in the lower left corner. The scarps and deposits of the three rock avalanche clusters are also shown.

3. The rock avalanche clusters

The rock avalanche deposits have been mapped and surveyed through a series of field campaigns (2011, 2012, 2014), aerial photo interpretation, sampling and testing. In this section, we describe for each rock avalanche of all clusters: the main morphologies, the external and internal structures of the deposits, the relationships among the multiple deposits and their relative ages and the computed volumes.

3.1. Scar areas

The scars of the northern and central rock avalanches groups are positioned in the upper part of the coastal scarp (Figs. 2 and 3). The northern rock avalanche scar is characterized by the coalescence of multiple scars of different geometry juxtaposed with each other. About 500 m to the north of the main scarp, another very large niche is present, with a total width of about 2 km, and with a maximum estimated recession of the scarp rim of about 600 m. The morphology of all these scars is strongly masked by aeolian deposits and sand dunes, making it difficult to identify the exact position for the scar toe. Regardless, the lower part of the mass, if present, was much thinner than the upper mass. Unfortunately, those aeolian sediments also mask most of the rocky outcrops at the sites, hampering a detailed analysis and rock mass characterization.

The central rock avalanche scar has an evident bowl shape, with a rounded upper scarp and well developed flanks. Some minor lateral levees are observed already within the scar area. A lateral levee, slightly masked by aeolian deposits and visible beyond the lower left hand flank of the scar, represents an interesting feature to describe the initial slope collapse (Figs. 2, 5). Locally, at the top of the scarp, vertical tension cracks (Fig. 4) cut through the alluvial subangular conglomeratic layers and are completely filled by thinly subvertical sheets of slightly cemented sands. This suggests a long history of slope instability followed by periods with colluviation of superficial deposits. Immediately to the north of the main scarp rim, we identified a rockslide with a marked main scarp (about 370 m wide and up to 15 m high, see Fig. 2c) and a longitudinal length of about 800 m. Direct field surveying does not show any recent evidence of displacement along this scarp. The open tension cracks, shown in Fig. 4, could be partially attributed to the joint effect of this instability and of the central cluster scar.

Finally, the southernmost rock avalanche shows a planar scarp surface probably controlled by a structural lineament which controls the entire slope, trending transversally (WSW–ENE) to the main coastal scarp (N–S). The scar has a V-shaped geometry, open towards the upper plateau area, suggesting a minor involvement of the lower slope sector in the failure.

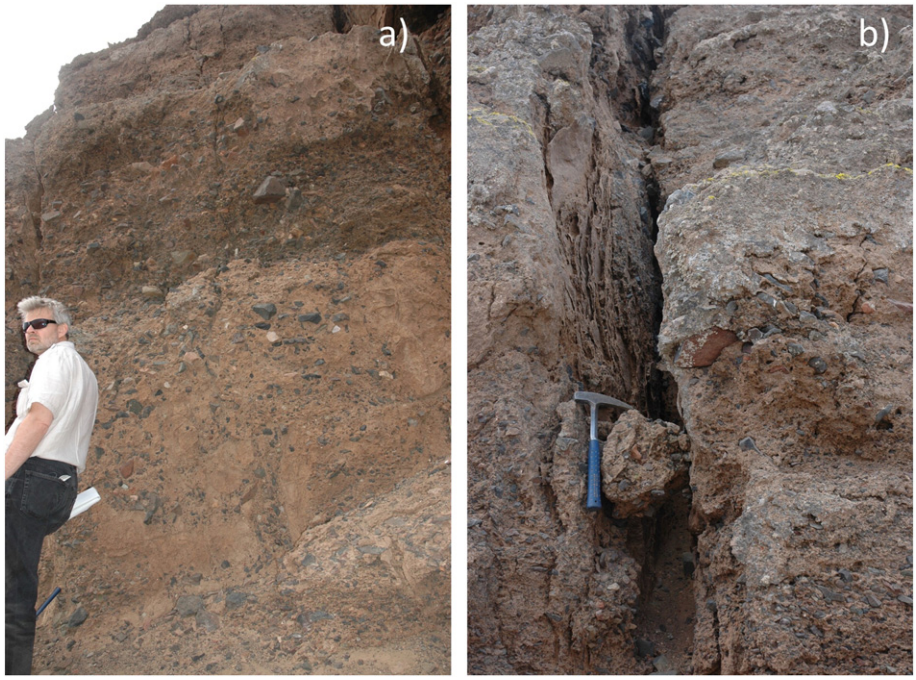

Fig. 4. Conglomeratic deposits close to the upper crest of the coastal cliff within the main scarp of the central rock avalanches group (see #4 in Fig. 2). A matrix supported structure with coarse polygenic clasts is visible, with subvertical cracks infilled by fine sands with thin vertical laminations.

3.2. Deposit characteristics

3.2.1. Morphometry

The rock avalanche deposits have been mapped and surveyed through a series of field campaigns to: verify their main characteristics, separate them by relative relationships and internal features, and gather observations about their grain size and characteristics. The main deposits have been subdivided in a sequence of smaller elements each one associated with an individual collapse. Successive field campaigns facilitated an improved characterization of the internal structures of the rock avalanche deposits by observation of newly excavated artificial outcrops.

Field surveys and remote terrain analysis of satellite imagery underline the presence of two sequences of landslide events. In both northern and central sectors, large volumes detached first, followed by multiple subsequent collapses, resulting in overlaying or directly confining deposits.

The deposits (Figs. 3, 4) are lobate in shape, characterized by sharp and relatively steep bulging fronts, and rear or tail sectors more depressed in thickness (or relative elevation above the peneplain) and generally delimited by well-developed levees (Fig. 6). The bulging frontal part is characterized by a convex geometry both in plan view and transversally, with longitudinal grooves and furrows slightly diverging towards the lobes limit, and oblique with respect to the lateral levees (Fig. 4). These features, clearly identified from satellite images, are consistent both in the main and secondary lobes. These longitudinal slightly diverging features converge uphill forming some sort of V-shaped pattern. The frontal lobes are affected by secondary instabilities in the form of rotational slumps (e.g. Fig. 6b: extreme left hand lobe in central cluster) and are partially concealed by aeolian deposits and some well-developed colluvial or outwash deposits. Behind the bulging front, a series of transverse ridges, slightly curved and often in the form of a hilly/hummocky terrain are recognized, with decreasing size uphill. Within the main lobes, some longitudinal shear features are recognizable. In some cases, especially for minor lobate deposits, the frontal bulging sector is completely isolated with no evident tail deposition excepted for some downhill concave well-spaced rib-like deposit and lateral levees (e.g. left hand secondary lobe in Fig. 6a, and right hand side and central part of the central rock avalanche cluster, Fig. 6b). Downhill concave ridges are present in the more distal portions whereas thin longitudinal ridges are evident upslope.

The straight lateral levees are both single and double ridged. At a larger scale (more detailed) they are slightly irregular, with shear structures cutting obliquely through them and causing slight lateral dislocations. Along the upper slope sectors the levees directly terminate or coincide with the lateral termination of the initial rockslide scar. Few exceptions exists and these are all associated with the largest lobes (i.e. largest failure volumes).

3.2.2. Internal structures

The internal characteristics of typical rock avalanche deposits have been observed at different sites. The structure and texture of the central rock avalanche deposit can be observed at the front of the central lobe where a small quarry with a vertical front extending about 130 m has been excavated (Fig. 7). At the same site, a small quarry for the extraction of guano was still active until 2013 then abandoned. These two excavations show the relationships existing between the underlying guano deposits, covering the bedrock, the rock avalanche accumulation and the aeolian sand deposits mantling the contact between the two. The vertical cut through the rock avalanche left hand lobe intersects four small longitudinal lineaments. Three main layers are recognized (see Fig. 7): a lower grey colored layer with abundant blocks in a very tight and close structure; an intermediate yellow to reddish colored layer, with finer matrix in the yellow bands and more blocky material in the upper red layer, including a 6 to 9 m thick blocky layer made of angular blocks, up to some meters in size, in a very tight arrangement and with a grain size in general coarser than in the other two layers. In this last layer, jigsaw blocks are visible with size up to a few meters as well as some thin red colored discontinuous layers. A slight upward coarsening and decrease in matrix content are recognized at the outcrop scale. The intermediate layer is characterized by a wavy geometry with very sharp crest geometries, a maximum thickness of about 1.7 m and a lateral extent of about 50 m. After the April 1, 2014 Iquique earthquake (M8.2), only some minor tension cracks were observed at the top of the quarry front, suggesting the high degree of interlocking and strength of the deposit.

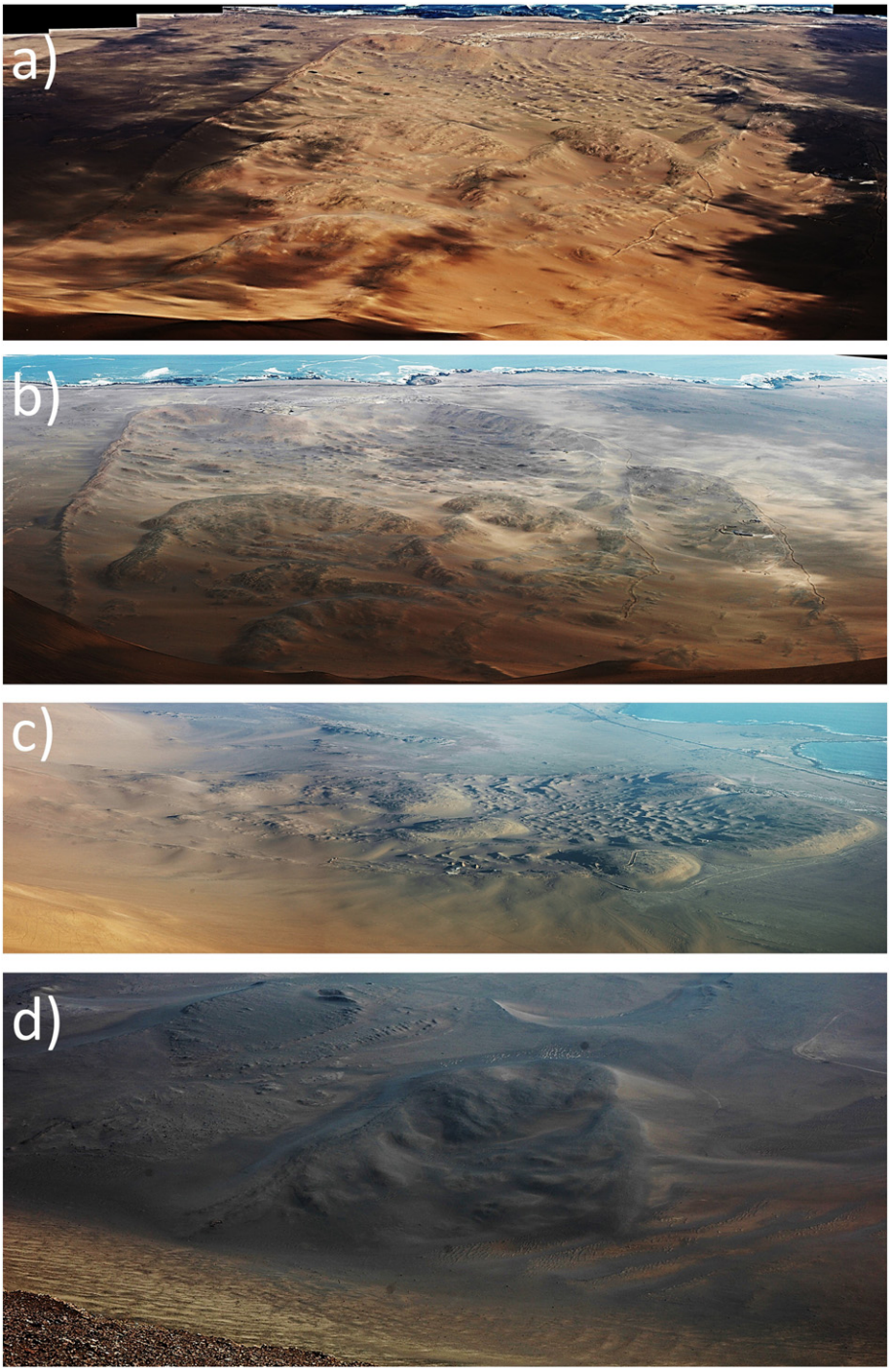

Fig. 5. Views of the three rock avalanches clusters: a) northern cluster seen from the scar; b) the depositional lobes seen from the scar, and c) central cluster (from the N); d) southern cluster (seen from the scar). See also Figs. 1, 2 and 3) and 9) for relative position.

The internal structure of the northern rock avalanche deposit (Fig. 8) was not visible till 2014, when a highway cut was excavated through the deposit exposing both the debris and the aeolian sands filling the depressions within the landslide deposit (Figs. 8a, b and d). The internal structures are similar to the previous ones. The material is tightly packed with levels or zones of different colors, from whitish to greyish and reddish. The blocks can be locally up to a few meters in size and their frequency increases towards the axis of the rock avalanche deposit. A thick lower layer of finer grain size can be observed at the right hand limit of the main lobe where red and grey colored layers are intercalated. In general, a coarser grain size is found in the central part of the deposit, with blocks of metric size (see Figs. 8a, b), whereas decimetric blocks are found close to the lateral boundaries and the levees (see Fig. 8d). No direct observation is available for the deposit characteristics at the very distal front. Furthermore, the left hand side of the rock avalanche is prevalently characterized by whitish-greyish colored deposits (see Figs 8a, b), whereas the central deposit and the right hand side are mainly formed by reddish rocks with some grey to green lenses (see Figs. 8c, d). Unfortunately, the basal layer is not visible at the site.

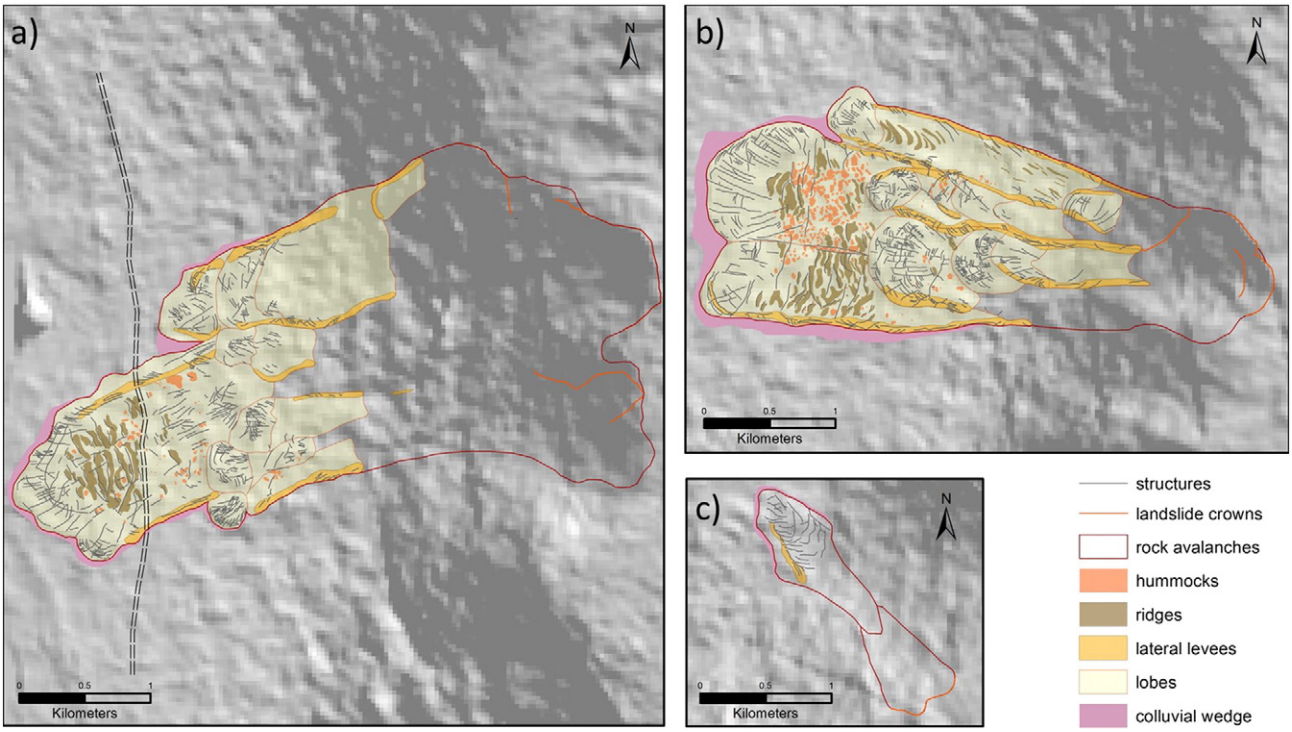

Fig. 6. Mapping of the main morphologic elements recognized within the deposits of the three rock avalanche clusters a) northern, b) central and c) southern, as from field surveys and aerial photo interpretation. The highway cutting through the main lobe of the northern avalanche cluster is shown.

4. Deposit dating

Each rock avalanche cluster is characterized by a series of events represented by distinct depositional lobes. Knowledge of the absolute age of individual landslide scars and deposits can be extremely useful for understanding both the failure and propagation mechanisms, the conditioning and potentially the triggering of events (e.g. Hermanns et al., 2000, 2001; Antinao and Gosse, 2009; Hermanns and Niedermann, 2011; Welkner et al., 2010). Thus the present level of hazard, as well as the interconnection between successive events, but also the

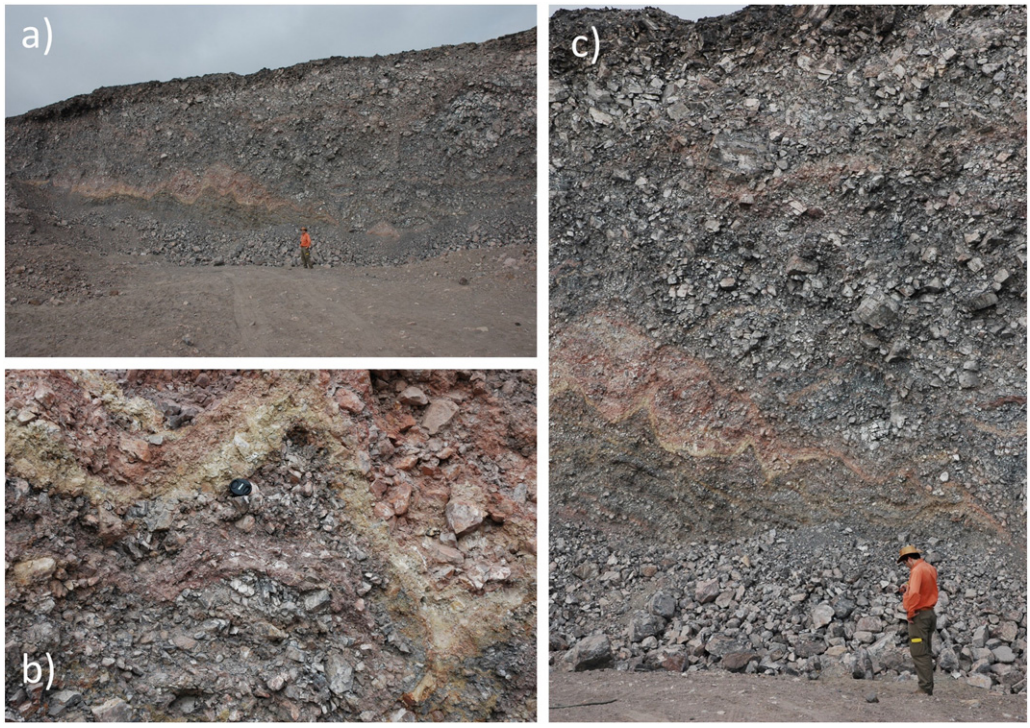

Fig. 7. Outcrop of the central rock avalanche deposit showing the internal structure in vicinity of the front of the left hand lobe (see #3 in Fig. 2). The three photos show the same outcrop at different degrees of detail. Three main layers are well visible: a lower grey to green grain-supported level with smaller clasts size, an intermediate yellow to reddish colored layer with wavy geometry, and a thick upper blocky layer with jigsaw blocks.

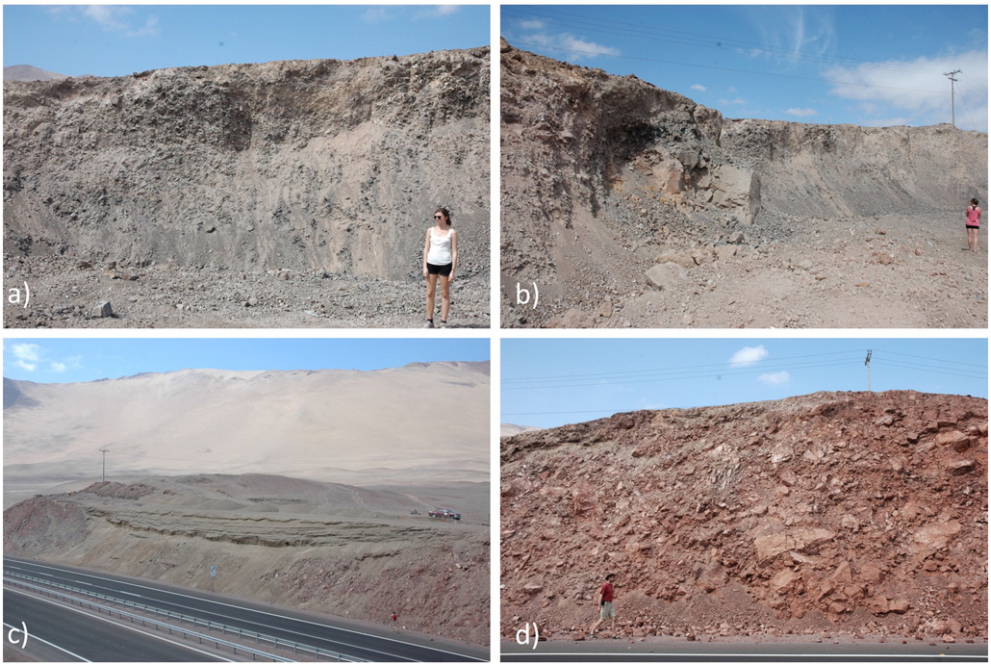

Fig. 8. Outcrop of the northern rock avalanche deposit showing the internal structure in the central part of the main lobe (see #1 and #2 in Fig. 2). A) left hand side characterized by grey dense sandstone blocks with a small percentage of matrix and rare large blocks (b); c) right hand side of the deposit with layers of different colors and aeolian sand deposits filling a depression of the rock avalanche surface; d) central sector of the coarse blocky deposit with reddish siltstones and sandstones.

relationships between occurrence and geological evolution of the main coastal scarp could be estimated. For example, dating the central cluster could give insight into recurrence intervals of strong earthquakes along the subduction zone. The large event deposits (both tsunami and landslides) are preserved within exposed Pliocene sediments of the coastal plain (Hartley et al., 2001). Quaternary marine terraces preserve remnants of sea-level maxima suggesting that landslides covering them can span an age range from 0.1 kyr^{-1} and possibly back to the mid Miocene (Mather et al., 2014). This is an extremely wide time range that we can try to define more precisely, recognizing a specific evolution of this area.

4.1. Relative dating

A relative dating of the events has been accomplished by analyzing the geometrical relationships among the various depositional lobes and levees identified within the rock avalanche clusters. Fig. 9 is a map showing the hierarchical subdivision of the main lobes. Each lobe (LN: northern lobe, LC: central lobe) is subdivided in secondary lobes (e.g. 3 for the northern cluster: LN1, LN2, LN3; 4 for the central cluster: LC1, LC2, LC3, LC4; 1 for the southern cluster: LS1; where number is associated to the occurrence order) and a further level of subdivision is proposed (n: northern, c: central, s: southern). The main criteria that we adopted for the subdivisions are: vertical superposition, runout distance, presence of well-defined levees associated to a frontal lobe, movement direction conditioned by the presence of antecedent deposits, freshness of the deposit, and finally the attribution of the originating scar area. From the map in Fig. 9, it is evident that larger events, characterized by a longer runout, are the oldest ones and a progressive decrease in volume is recorded for the successive events. This will be recalled and used in the next sections relative to the slope stability and the runout assessment.

4.2. Absolute dating

No single, ideal dating method could be used on all deposits due to problems such as lack of organic material, too high ages to be determined with the ^{14}C method, absence of sand dunes on several of the rock-avalanche lobes and unfavorable fragile source rock resulting in a small boulder size on top of the rock-avalanches deposits. A combination of various dating methods was tested in order to obtain a good understanding of the temporal distribution of events. As a consequence, 19 samples were examined: 3 samples for ^{14}C dating of organic material in stratigraphic relation with rock-avalanche deposits, 4 samples for optical stimulated luminescence of aeolian deposits overlying the rock-avalanche deposits, and 12 samples for cosmogenic radionuclide datings of boulders from the top of the central rock avalanche cluster. Samples were collected in successive campaigns as ^{14}C dating of several samples from marine terraces revealed them to be too old. Samples for optical stimulated luminescence dating were extracted by trench digging (see Figs. 11a, b) through the colluvial wedges deposited along the border of the rock avalanche deposits. This is a difficult task to be accomplished in such environment because of the presence of loose sands and colluvial wedges that locally can reach important sizes. Samples for cosmogenic radionuclides dating were collected by sampling the largest blocks assuming that they were never covered by other rock avalanche material or Aeolian deposits. However boulder sizes were between 30 and 200 cm in diameter only with most of the boulders not exceeding a diameter of 60 cm.

4.3. ^{14}C dating of organic material stratigraphically related to rock avalanche deposits

^{14}C dating was applied to all organic materials that were found in stratigraphic relation to rock-avalanche deposits. These are stratified marine deposits 8 m above the present sea level containing shells (Fig. 11b) overlying the frontal parts of the largest and lowermost rock-avalanche deposits of the northern cluster. These result in an age of 40,690 ± 520 yr BP (conventional radiocarbon age, Beta – 307,649) and thus representing a minimum age of that deposit (see Fig. 10).

The largest and lowermost rock-avalanche deposits of the central cluster are underlain by a marine terrace containing guano deposits. Two shell fragments were separated from the guano and dated to > 43.500 yr BP (conventional radiocarbon ages, Beta – 307,646, Beta – 307,648) giving a minimum age for that deposit (Fig. 10). Taking into account the uplift rate determined for this part of the Chilean coast for

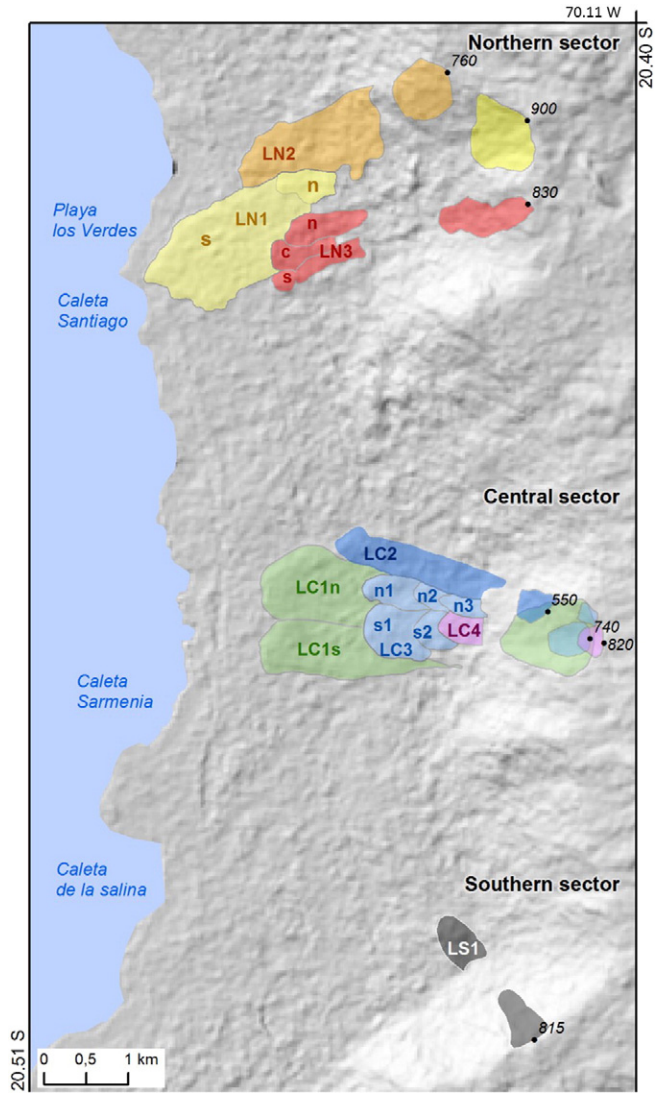

Fig. 9. The northern (N), central (C) and southern (S) rock avalanche clusters subdivided in a sequence of depositional lobes. Numbers give the relative order of occurrence and small letters (n, c, s) the relative position within the deposit. The labelled deposits are those used in the successive slope stability analyses and runout modeling. To each lobe a probable originating scar is associated and represented with the same color.

the past 40 kyr (see below) this age could be as much as several 100 kyr too young. This is the lowermost of five marine terraces in the study area and vicinity that were also sampled for ^{14}C dating (Fig.10). However, as the lowest terrace resulted in an age too old to date with that method samples from higher terraces were not analyzed.

4.4. Optical stimulated-luminescence dating of aeolian deposits overlying rock avalanche deposits in the northern, central and southern cluster

Sand dunes cover rock avalanche deposits and are ideal deposits to apply optical stimulated luminescence dating. In order to extract samples for this dating technique trenches were hand excavated into overlying sand dunes/aeolian deposits down to very angular talus deposits of re-deposited rock-avalanche material (i.e. colluvial and outwash deposits) along the margin of the deposits. Samples were taken by hammering plastic pipes (see Fig. 11a) into the lowermost sand layer covering the talus in order to prevent exposure of the sample to the sunlight and thus resetting of the luminescence signal. Samples were submitted to "The Nordic Laboratory for Luminescence Dating, Department of Earth Sciences, Aarhus University." Results obtained represent average ages of multiple single grain dating of quartz minerals and range from 4200 ± 400 yr to 30,000 ± 2000 yr. These ages represent minimum ages of the respective deposits as the sand dunes overlie the deposits and there is no control of how far from the true age that minimum age is at each location. However, the ages correspond to the stratigraphic position. (see Fig. 10, Table 1).

4.5. Terrestrial cosmogenic nuclide dating

Terrestrial cosmogenic nuclide (TCN) dating was used on the central cluster in order to validate the relative ages of the deposits. For this, the top surfaces of the largest boulders on each lobe were sampled with a chisel. Boulder size was noted to be significantly less than in the cuts into the deposit and are summarized in Table 2. Boulders of pre-historic rock avalanche deposits have been previously dated by Hermanns et al. (2001, 2004), Ivy-Ochs et al. (2009), Antinao and Gosse (2009), demonstrating the applicability of this method to such a phenomenon.

In total, six lobate deposits have been sampled (see Fig. 10) by collecting two samples from each lobe. The samples were collected following the recommendations of Gosse and Phillips (2001), recording the rationale for sample selection, description of sampled failure surface, geologic description of sample, location, orientation, sample thickness, and shielding geometry. The samples were prepared and ^{36}Cl concentrated at the Dalhousie University Cosmogenic Nuclide Exposure Dating Facility in Halifax, Canada. Total Cl and ^{36}Cl were determined at the PRIME accelerator mass spectrometry facility at Purdue University in Indiana, USA. The derived ages were calculated using the program CRONUS ^{36}Cl exposure age calculator (Balco et al., 2008) and therefore were calculated using global production rates and scaling models by Lal (1991) and Stone (2000). A comprehensive review of TCN dating is provided by Gosse and Phillips (2001). Data used for the age calculation are given in the supplementary material (Suppl. Table 1).

Results from the dating are presented in Table 2 with 0 and 1 mm/kyr erosion rates and with 1 mm/kyr erosion rates in Fig. 10. Ages assuming 1 mm/kyr erosion rate obtained spread from 33.7 ± 5.1 to 138 ± 28 kyr. However, the youngest and oldest ages belong to the same lobe, LC 4, which is stratigraphically the youngest lobe. This lobe, LC 4, is also the smallest deposit that does not exceed the travel or reach angle of rock falls. Hence these ages might represent the age of rock falls postdating the rock avalanche. In case that the rock fall originated from the top of the scar the boulder is likely to have an inherited age due to pre-exposure on the scar. All other ages spread from 52.5 ± 7.7 to 69 ± 11 kyr and the ages of the different lobes are indistinguishable within uncertainty margins.

Dating of the marine deposits overlying the largest rock avalanche lobe in the northern cluster, at an elevation of about 8 m a.s.l., allows us to compute the tectonic uplift rate. This results in a value of 0.2 mm/yr for the last 40 kyr.

4.6. Datings and reconstruction of the rock avalanches sequence

The absolute datings (see Figs 10a, b, Fig. 12, and Tables 1, 2) suggest a series of interesting conclusions:

- The central cluster seems to be the oldest one. ^{14}C data show ages beyond the technique limits (43,500 BP): Thus the true age is older than that. This coincides with the cosmogenic dataset. TCN ages are indistinguishable and cluster around ~60 kyr, thus the ^{14}C age supports the cosmogenic dataset. Unfortunately, due to the large uncertainty brackets and very similar ages, the TCN data do not indicate if rock avalanche events have been separated in time by thousands of years or by much smaller intervals. These results are thus very different from the results of TCN dating of a similar rock avalanche cluster further east within the Puna plateau (Hermanns et al., 2001).
- The northern cluster has been dated by means of optical stimulated luminescence and ^{14}C analyses. Both techniques give relative recent ages, ranging between 4 kyr and 40 kyr. As a consequence, these

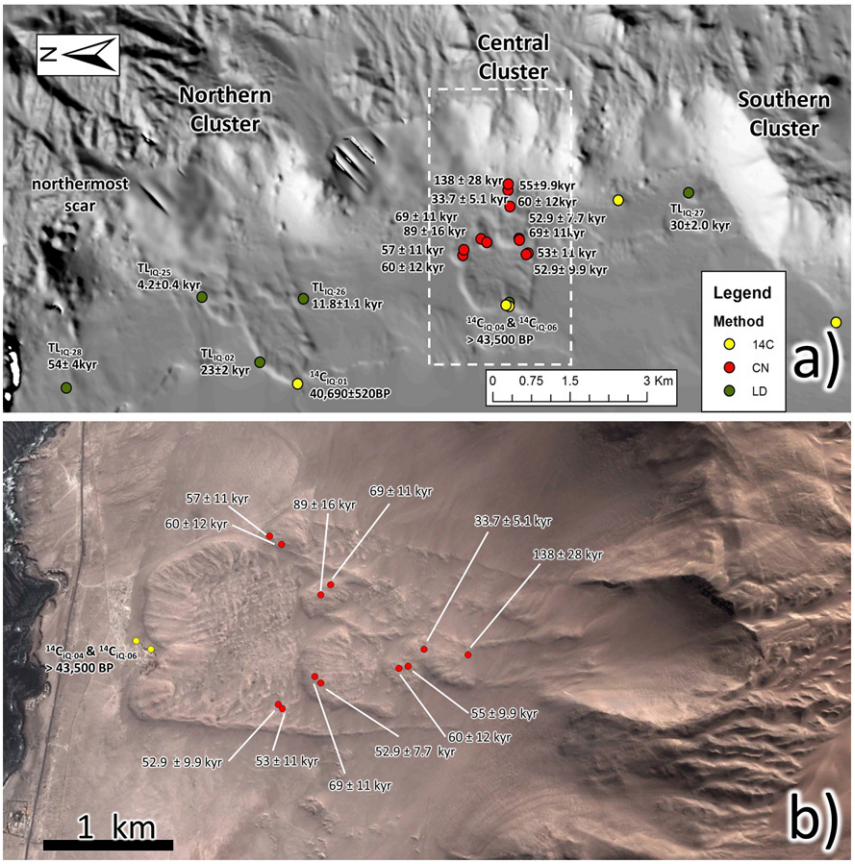

Fig. 10. Hillshade model of a) the three rock avalanches clusters with the location of the collected samples and the results of the relative datings. The large scar to the north of the northern cluster is also evidenced. The dashed rectangle points at the limit of figure b) image of the central cluster with the exact location of samples and the relative ages.

events are more recent than those of the central cluster. The largest lobe (LN1 in Fig. 9) can be dated back to a minimum age of 40,250 BP on the basis of the ^{14}C dating (Fig. 10). This seems very roughly confirmed by an optical stimulated luminescence minimum age of about 23 kyr. The LN2 and LN3 (in particular LN3s) lobes have minimum ages of 11.8 kyr and 4.2 kyr, respectively and thus coinciding with their stratigraphic position. However, similar to the minimum age of lobe LN 1, this may be >10 kyr too young. It should be noted that the LN3 lobe seems to be associated with a scar located slightly outside the main scar from which LN1 and LN2 probably originated.

- The southern rock avalanche, deposited on the upper marine terrace, dates back to a minimum age of 30 kyr on the basis of optical stimulated luminescence analyses. Considering that we have no independent age control on that cluster and that the optical stimulated luminescence age of lobe LN1 postdates its real age by 17 kyr, this cluster could either be as old as the northern or the central cluster.

5. Rock avalanche volumes

After having determined the relative and absolute order of occurrence of the collapses, and having recognized the direct relationship between age and volume, it is important to estimate a reliable value for the volume of each event (i.e. lobe). This information will be relevant for the analyses in the following sections of the manuscript.

Fig. 11. a) Lateral view of a trench dug through the N-flank of the northern cluster for optical stimulated luminescence dating. The rock avalanche deposit is covered by a colluvial layer and sand aeolian deposits. b) view of the outcrop (ca. 8 m a.s.l.) at the front of the northern cluster where samples have been collected for ^{14}C dating; c) outcrop located along the coastline at the front of the large empty scar just north of the northern cluster. Large rounded and brecciated materials are observed and could be associated to an old rock avalanche completely reworked by the ocean.

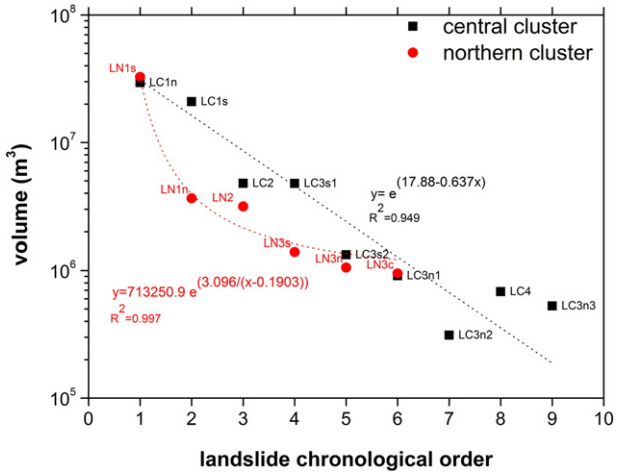

Fig. 12. Plot of the rock avalanche volume, both for the northern and central clusters, with respect to the relative chronological order of detachment as from mapping and field surveys. To be compared to Utili and Crosta (2011).

The volume estimates require the integration of data collected by remote terrain analysis of satellite imagery, field geomorphological mapping, sedimentological, geological and structural data collection. For a reliable estimate of the volumes, a detailed topographic description of the area is required. In order to obtain this, a high resolution 2 m × 2 m DEM model has been generated for the entire area starting from high resolution Geoeye images.

The volume estimate also requires the definition of a pre-collapse topography. This has been reconstructed by extrapolating below the deposits the topography in their immediate vicinity using deposit and levee thicknesses (therefore levee volumes) as from field observations and DEM evidence. By subtracting the pre-failure to present day generated DEMs we computed the deposit volumes.

Reconstruction of the pre-failure topography at the scar sites, by using the slope geometry in the immediate vicinity, allows an estimate of the volume of the released mass to compare with volumes of related deposits. The rock avalanche volumes range between 180,000 m^3 and 29 million m^3. These landslides ran out over guano deposits and Pleistocene marine terrace deposits which cover the coastal plain. The lobes have been partially smoothed by aeolian deposits (see Fig. 8c as an example for lobe LN1), possibly causing an imprecise computation of the volumes. Along the lobe limits, colluvial wedges made of rock avalanche material are present below the aelioan sandy deposits. The values of the computed volumes for both the scar and the deposit of each recognized event are summarized in Table 3.

Again, the observation of slope morphology, the reconstruction of topographic surfaces and the quantitative estimate of volumes show an evident relation between landslide volume and assigned order of detachment (see Table 3 and Fig. 12). In both sectors, big landslides detached first, reaching longer distances, followed by other events progressively diminishing in dimensions and in total runout.

The volume versus chronological order relationship looks promising even in presence of the already recalled uncertainty which can be associated with the presence of aeolian deposits covering the rock avalanches (major problem for large events) and errors in the extrapolation of the basal surface below the rock avalanche lobes and levees. These errors could be more relevant for the case of the northern cluster, considering the abundance of aeolian deposits along the slope (see dunes in Fig. 3b), in the main scar area and in the lower sectors. A rough estimate of the associated error can be found in Table 3, where the differences between the computed lobe volumes and the corresponding scar volumes are reported. The reasons for the differences could be: bulking of the rock avalanche material, partial mantling of the lobe limits and scars by aeolian deposits; presence of paleomorphological features in the deposition area which cannot be easily eliminated; irregular slope crest geometry which has been linearized for the volume reconstruction; influence of rock mass bulking during transport; difficult computation of levee volumes.

6. Rock avalanche mobility

Studies on rockslide-avalanche dynamics have related landslide runout to an apparent friction coefficient, defined as the tangent of the slope connecting the pre- and post- collapse centers of gravity of the rock mass. As proposed by Heim (1932), since the pre-landslide topography is quite difficult to reconstruct with a good precision, the coefficient can be approximated to the tangent of the slope joining the scar high point to the furthest point (tip) reached by the landslide, dividing the fall height H by the horizontal runout L (Heim's ratio). Scheidegger (1973) and Ui (1983) noticed that a direct relationship exists between landslides volume (V) and the ratio H/L, which decreases systematically with volume increase. This observation, confirmed by other researchers studying rock and debris avalanches in different environmental and geological conditions, is confirmed in the present study (Table 3 and Fig. 13).

In order to find a realistic and consistent basal friction angle for each of the considered landslides within each of the two main clusters, H/L ratios were related to landslide volume, and fitted (Fig. 13a).The corresponding values of the apparent friction coefficient represent the tangent of a specific basal friction angle, φ_b (Table 2).

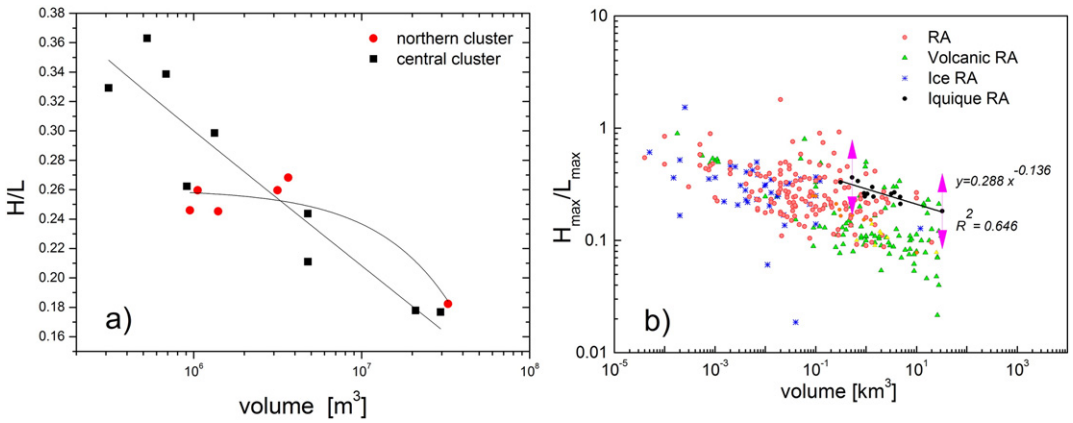

Fig. 13. a) Plot of H/L versus volume for the various rock avalanches and the best fitting logarithmic relationship; b) same plot as in a) but representing also most of the well supported data published in the literature (updated after Sosio et al., 2012).

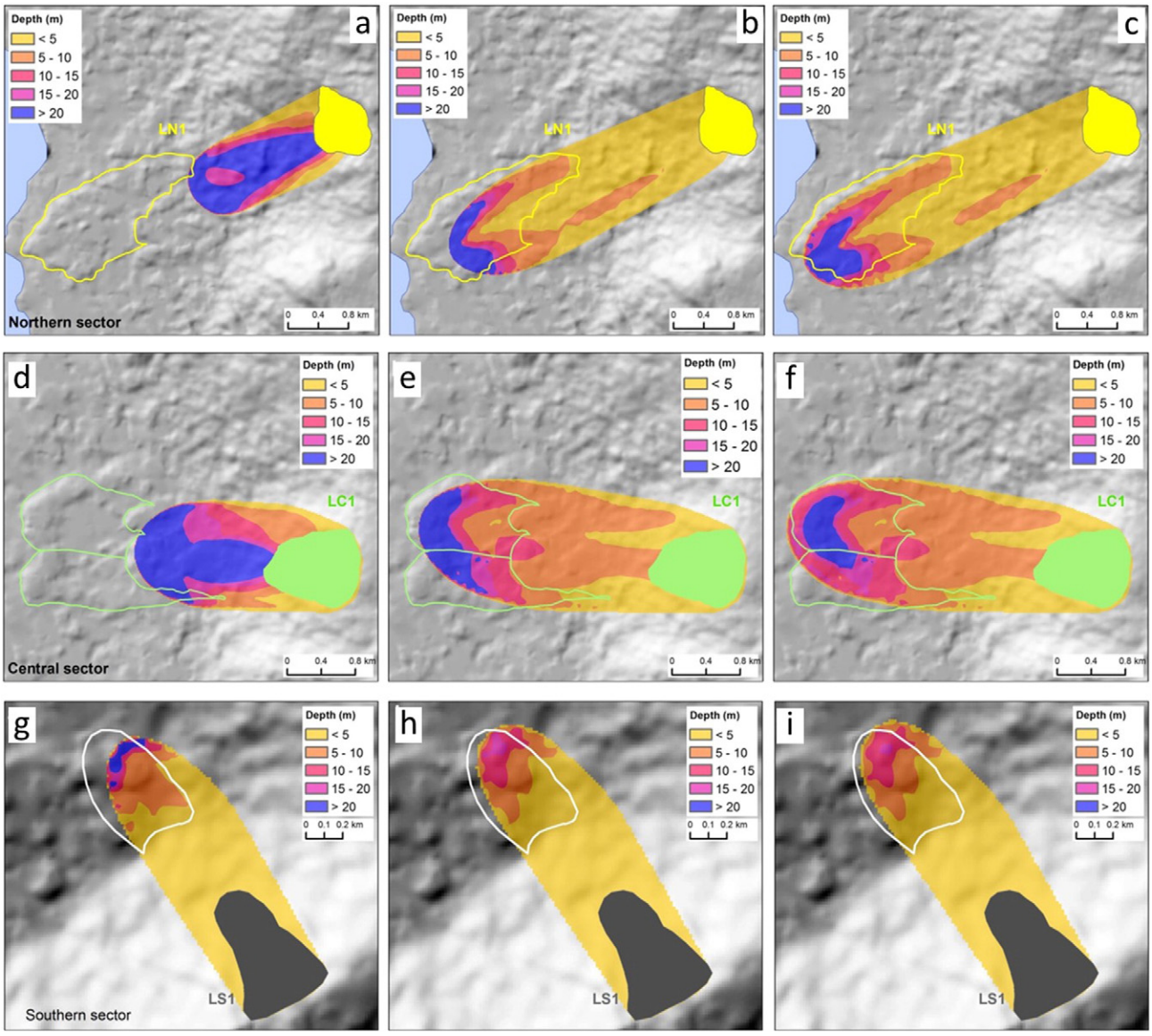

Fig. 14. Time evolution of rock avalanche a–c) LN1 (northern cluster), d–f) LC1 (central cluster) g–i) LS1 (southern cluster) after 30 s (a, d, g), 60 s (b, e, h) and at stop (c, f, i). (Source areas as in Fig. 9.)

7. Slope stability analyses

In the pre-failure stage, the global slope stability can be expressed through a factor of safety, which normally is calculated by means of limit equilibrium analyses. Three dimensional slope stability analyses were performed based on the extension of four standard limit equilibrium methods to three dimensions. Among them was Bishop's Simplified Method, as modified by Fredlund and Krahn (1977), making the method applicable to non-rotational geometries, within limitations suggested in Hungr et al. (1989). The slope stability analyses allowed the identification of the most probable rupture surfaces, also by direct comparison with topographic data and field observations, helping in the reconstruction of post-landslide topographies for each event. The available geometrical, physical mechanical data and field observations concerning the rock lithology (conglomerate, marl, schist, and limestone), and the degree of fracturing and weathering, suggested a certain homogeneity of the source materials. These have been assigned an internal friction angle ranging between 30° and 35°, a constant bulk unit weight of 25 kN/m^3, and a cohesion ranging from 100 to 300 kPa (Table 4). These values are those adopted in the back analyses of slope

Table 1
Optical stimulated luminescence ages of quartz grains extracted from samples taken in plastic tubes hammered into sand dunes overlying rock avalanche deposits.

Sample	Lobe	Lat [dd]	Long [dd]	Depth [cm]	Dose [Gy]	Number of grains	Dose rate [Gy/kyr]	Water content [%]	Age [kyr]	Uncertainty 1 sigma [kyr]
IQ-02	LN 1	−20.4078	−70.16042	90	40 ± 3	22	1.78 ± 0.12	7	23	2
IQ-03	LN 1	−70.1487	−70.15012	40	14.6 ± 1.1	24	3.64 ± 0.17	3	4	0.4
IQ-25	LN 2	−20.3977	−70.14870	70	10.6 ± 0.8	24	2.52 ± 0.11	7	4.2	4
IQ-26	LN 3	−20.4156	−70.14918	40	35 ± 3	28	2.94 ± 0.14	7	11.8	1.1
IQ-27	LS 1	−20.4833	−70.13071	55	72 ± 4	27	2.36 ± 0.11	8	30	2

Table 2
^{36}Cl exposure ages for samples on the central rock avalanche cluster (ε is the erosion rate, σ is the standard deviation). Sample locations are displayed in Fig. 10.

Sample	Lobe	Location		Elevation	Boulder size	^{36}Cl age	Ext. unc.	^{36}Cl age	Ext. unc.	Deposit mean age	Uncertainty
		Lat	Long		Longest axis	ε = 0		ε = 1 mm / kyr		ε = 1 mm/kyr	
		[dd]	[dd]	[m]	[m]	[kyr]	[1σ kyr]	[kyr]	[1σ kyr]	[kyr]	[1σ kyr]
IQ 13	LC 1 s	−20.4551	−70.1413	144	0.8	59	11	53	11		
IQ 14	LC 1 s	−20.4548	−70.1413	183	0.4	60	10	52.9	9.9	53	10.5
IQ 15	LC 2	−20.4436	−70.1416	188	0.6	73	17	60	12		
IQ 16	LC 2	−20.4438	−70.1406	146	0.6	67	14	57	11	58.5	11.5
IQ 17	LC n1	−20.4468	−70.1387	116	0.3	81	14	69	11		
IQ 18	LC n1	−20.4478	−70.1393	114	0.4	100	17	89	16	79	13.5
IQ 11	LC s1	−20.4535	−70.1387	87	1.0	55.9	7.5	52.5	7.7		
IQ 12	LC s1	−20.4536	−70.1389	84	0.5	79	14	69	11	62	9.9
IQ 07	LC s2	−20.4520	−70.1330	91	0.3	69	15	60	12		
IQ 10	LC s2	−20.4517	−70.1290	90	2.0	60	10	55	9.9	57.5	11
IQ 08	LC 4	−20.4517	−70.1301	82	0.4	36.6	5.6	33.7	5.1		
IQ 09	LC 4	−20.4516	−70.1290	88	0.4	160	30	138	28		

stability and the critical values are shown in bold in Table 4. The different failure phases have been analyzed in chronological order (as presented before), using, for each subsequent stability analysis, the actualized slope geometry. The actualized slope geometry was derived by subtraction of the "destabilized" mass from the initial topography (i.e. DEM). The ongoing calculation geometry was thus updated according to the previous calculation results.

8. Runout numerical modeling

The numerical modeling of landslide runout has been performed through the use of the code developed by Chen and Lee (2000) to simulate debris flows, avalanches and fast moving long runout landslides (Crosta et al., 2004, 2006). The solution is formulated with the finite element method in the Lagrangian reference frame. The simulation parameters were calibrated through a back analysis of the slope failures as identified in the previous sections, on the basis of geometry of the transportation and deposition sectors and thickness. For each landslide simulation, the pre- and post-failure topographic surfaces have been used, with a ground resolution of 15 m × 15 m. The horizontal projections of the source areas were discretized into quadrilateral unstructured meshes. The nodal values of material thickness were obtained by interpolation of the difference of the pre- and post-topographic surfaces. The basal rheology to be used in the simulation is assigned through a set of parameters, depending on the selected rheology, which has been adjusted by trial and error during the calibration procedure. Frictional and Bingham rheological models were alternatively considered for basal shear stress in this study. The frictional rheology assumes the basal shear resistance, τ, to depend only on the effective normal stress, σ. The frictional equation is expressed as, $\tau = \sigma_z (1 - r_u) \tan\varphi$, where the pore-pressure ratio, r_u, and the dynamic friction angle, φ, are the parameters to be introduced in the model. Both of them can be alternatively expressed by the basal friction angle, $\varphi_b = \arctan(1 - r_u)\tan\varphi$.

For the simulation of the Iquique rock avalanches, a constant bulk unit weight of 25 kN/m^3 was considered, and an internal friction angle of 35°, as resulting from slope stability analyses. Basal friction angle for each landslide was initially assumed equal to the H/L ratio (see Table 3), so as to have a reasonable value to start the successive calibration phase. The lateral earth pressure ratios were calculated according to the Savage and Hutter's (1989) approach.

Bingham's rheological model combines plastic and viscous behavior. A Bingham material behaves as rigid below a threshold yield strength, and as a plastic one above it. The basal shear resistance in this case is calculated from (Hungr and McDougall, 2009):

$$\tau^3 + 3\left(\frac{\tau_{yield}}{2} + \frac{\mu_B v_x}{h}\right)\tau^2 - \left(\frac{\tau_{yield}}{2}\right)^3 = 0$$

Bingham model best simulated the real behavior of the Iquique landslides (see Figs. 14a, b and c, for results of lobes LN1, LC1 and LS), showing that in these cases basal resisting force is a function of flow depth, velocity, constant yield strength (τ_{yield}) and dynamic viscosity (μ_B). The best performance of the Bingham model is validated by comparing geometry of the deposit, in terms of longitudinal and transversal extent, lobe plan geometry and thickness against the real observed ones. As

Table 3
Main values of the geometrical characteristics of the rock avalanches recognized within each cluster. Scar and deposit volumes were computed by generating a pre-failure DEM. The landslide names correspond to those reported in Fig. 9. The percent change in volume for the scar and deposit estimates is reported. Cells with the same values means that for minor or secondary lobes no trial has been done to obtain more refined estimates and the subgroup of lobes has been considered as a single event.

Landslide	H/L	H/L fitted	φ_b °	Area m^2	Deposit Volume m^3	Scar volume m^3	Difference %
LC1n	0.177	0.165	9.4	1,001,836	38,109,817	29,493,965	22.6
LC1s	0.178	0.179	10.1	932,891	27,054,559	20,938,075	22.6
LC2	0.211	0.238	13.4	666,974	5,981,625	4,783,725	20.0
LC3s	0.244	0.238	13.4	526,165	9,446,858	6,106,351	35.4
LC3s	0.299	0.289	16.1	526,165	9,446,858	6,106,351	35.4
LC3n	0.262	0.305	16.9	415,292	647,485	1,748,966	170.1
LC3n	0.329	0.347	19.2	415,292	647,485	1,748,966	170.1
LC4	0.339	0.316	17.5	161,531	952,489	683,550	28.2
LC3n	0.363	0.326	18.1	415,292	647,485	1,748,966	170.1
LN1	0.182	0.157	8.9	1,890,541	35,842,188	36,313,117	1.3
LN1	0.268	0.249	14.0	1,890,541	35,842,188	36,313,117	1.3
LN2	0.260	0.255	14.3	1,160,747	3,012,332	3,152,363	4.7
LN3s	0.245	0.287	16.0	682,960	4,055,058	3,398,589	16.9
LN3n	0.260	0.299	16.6	682,960	4,055,058	3,398,589	16.9
LN3c	0.246	0.303	8.9	682,960	4,055,058	3,398,589	16.9
LS1	0.379			237,840	150,727	192,821	

Table 4
Values of the safety factor for automatic search rupture surfaces, and related model parameters. Kh is the coefficient of horizontal acceleration adopted in the analyses and expressed in fraction of g. In bold are the most critical conditions (i.e. closest to the critical value of 1).

#	Cohesion kPa	Int. friction angle °	Kh	Central sector					Northern sector		
				LC1	LC3n	LC3s	LC2	LC4	LN1	LN3	LN2
1	100	30°	0.3	0.77	0.68	1.00	0.78	0.61	0.82	0.80	0.74
2	100	35°	0.3	0.90	1.12	1.12	0.90	0.65	0.90	0.92	0.86
3	100	30°	0.4	0.66	0.58	0.93	0.67	0.53	0.71	0.68	0.67
4	200	30°	0.4	0.78	0.81	1.18	0.83	0.68	0.89	0.80	0.82
5	200	30°	0.3	0.76	**0.98**	**0.99**	**0.97**	**1.02**	0.87	0.79	0.85
6	**300**	**35°**	**0.4**	**1.01**	1.64	1.65	1.09	0.82	**1.14**	**1.04**	**1.04**

earth pressure yield criterion, the hydrostatic assumption was held, considering the six lateral earth pressure ratios (in terms of active and passive states along the locally dominant transversal flow direction) equal to one. Again, a constant bulk unit weight of 25 kN/m^3 was assumed in all the analyses.

Taking advantage of the reconstruction of all the successive phases presented in the previous sections, each landslide was modelled consequentially, following the chronological order. Therefore, the topographic surface obtained by the previous one after deposition of the antecedent rock avalanche was used for each simulation. For back analysis, yield strength τ and dynamic viscosity μ needed to be determined. In Bingham model, however, yield strength mainly influences the thickness and runout, making rather trifling the changes in dynamic viscosity. In Table 5, model parameters producing the best correlations between computational results and field observations are presented. The LC3s and L4 events have not been simulated because of the problems relative to the poor geometrical characterization of the source areas.

9. Discussion

The identification of clusterized slope instabilities can be useful to assess the main controlling conditions which make some areas more susceptible to instability, or to identify the potential triggering mechanisms and their recurrence in time (e.g. Strom, 2015). In the study area presented here, three clusters of rock-avalanche deposits have been identified, mapped and characterized. This area is one of the most seismically active in South America and is characterized by extremely dry conditions. The central cluster was initially identified by Novoa (1970) and recently discussed by Yugsi Molina et al. (2012a, b), Crosta et al. (2012) and Mather et al. (2014). Nevertheless, two more clusters had never been previously identified even though positioned nearby and with the same main characters. This coincidence suggests the presence of particular conditions which controlled the triggering and evolution of the rock avalanches characterized by very similar morphologies and mobility. For the two main clusters (N and C) we mapped a sequence of many events, always characterized by a progressive decrease in volume. This observation is in agreement with numerical and analytical slope stability analyses presented by Utili and Crosta (2011). They showed that a logarithmic relationship exists between the unstable block area (in two dimensions) and the order of collapse (i.e. cumulative frequency of failure events) in relation both to differential initial topographic gradients and to internal friction angles. In this way we confirm the trend in volume release that can be associated to a specific source area, because of the progressive tendency to reach a final and more stable slope profile.

Relative dating of the events within each cluster allowed us to reconstruct the relative relationships and the geometrical conditioning in the evolution of the entire sequence of phenomena. The persistence of the instabilities at the same exact locations can be attributed to the presence of initially weakened rock masses (e.g. cataclinal dipping), to local steeper morphologies, to proximity to the epicenter (or source zone) of large magnitude earthquakes, to recurrent seismic events, and to slope orientation with respect to the direction of wave propagation (Bouchon et al., 1996). At the same time, it is difficult to determine if these events were simultaneous, in the sense of a very condensed and continuous sequence, or if they resulted from events distributed over several thousand to more than 10 thousand years. In this case they would be much shorter spaced in time than very similar rock avalanche clusters along the eastern slope of the Andes bordered by piedmont terrains and in the intra Andean Puna plateau at about the same latitude, and non-glaciated Andean valleys with small catchments (Hermanns et al., 2000, 2001, Moreiras et al., 2015). Furthermore, these are certainly different from glacially eroded valleys further south in the Central Andes and on the border between the Central and the Patagonian Andes (Antinao and Gosse, 2009; Welkner et al. 2010; Penna et al., 2011; Hermanns et al., 2014). Lobe and levee geometries remain very much the same and the internal structure of the northern and central clusters are quite comparable in terms of degree of fragmentation, compaction and grain size distribution of the fragments. Also, the general geometrical and depositional characteristics suggest the persistence of similar environmental conditions, both in terms of landslide material behavior and of the material forming the basal substrate. At the same time, the rock avalanche deposits are well preserved, apart from the masking action of aeolian deposits, and the frontal part of the lobes is perfectly preserved. This excludes the reworking action by the ocean waves and therefore the possibility of these rock avalanches having been deposited in shallow water conditions (i.e. with a coastal plain partially submerged) or in wetter periods when water runoff should have incised the deposits.

A special case is represented by the northernmost niche, just north of the northern cluster, to which we have not been able to associate a real deposit. Nevertheless, along the coastline just in front of this scarp a well preserved outcrop of brecciated materials with subangular to rounded shapes has been found (see Fig. 11c). These materials suggest that a very old rock avalanche event occurred when the coastal plain was still covered by water and wave action could have strongly reworked the deposit leaving only few remnants of the original.

The absolute datings for some of the lobe deposits, by optical stimulated luminescence, ^{14}C and cosmogenic radionuclides, embrace a time span between 4 ± kyr and ~60 ± 10 kyr. The central cluster seems to have originated well in advance of the other two, with a complete emptying of the source area occurring over only a few kyr, with a sequence of events characterized by a logarithmic decrease of volume. Some of the lobes can be characterized by anomalous absolute dates, with respect to the assigned relative order of collapse, but this could result from erosion of older material lying along the basal surface. In fact, it is common for such processes to erode material and to push it in front of the moving mass. In our case, eroded material could pertain both to the basal layer and to the material deposited in the levees by previous events and eroded by the successive rock avalanches, which were laterally confined during their motion. Unfortunately, the best places to find and sample large blocks for cosmogenic nuclide dating are located within the frontal part of the deposits, where it is also easier to find recycled materials or large blocks expelled from the moving front, or at the tail of the deposit where large block can be the result of large rockfalls.

The northern cluster became active after the end of the activity of the central one, between 40,000 ± BP and 4 ± kyr and at the same time the southern cluster was activated. Again, for this northern cluster, each one of the rock avalanches behaved in a similar way. It must be noted that some of the events where characterized by the deposition of the entire mass in a convex and regular shape with no upslope elongation of the deposit but only with the presence of well-developed lateral levees.

On the basis of the computed volumes and of the absolute dating we can provide a rough estimate for the sediment yield from this sector of the coastal scarp with an approximate total length of about 15 km. The present elevation of the toe of the main lobe is about 55 m a.s.l. At

Table 5
List of the values for the Bingham model parameters as obtained from the model calibration for each one of the rock avalanche lobes forming the two main clusters.

Sector	Landslide	T_{yield} (kPa)	μ_B (kPa·s)
	LN1	52	0.8
North	LN2	78	0.8
	LN3	50	0.8
	LC1	75	0.8
	LC2	15	0.8
Central	LC3n	1	0.4
	LC3s	–	–
	LC4	–	–
South	LS1	50	0.8

the present day average uplift rate (ca 0.06–0.34 mm/yr, Quezada et al., 2006; 0.25–0.3 mm/yr; Regard et al., 2010) a total time of about 225,000–550,000 yr is required to reach this elevation assuming an uplift rate of 0.2 and 0.1 mm/yr, respectively. Therefore, at the time of occurrence of the main rock avalanche in the central cluster (60 ± 10 kyr) the coastal plain should have been about 12 m above the present day sea level, and so away from possible wave reworking Uplift rate calculated from dating of the marine and aeolian deposits that overly the northern rock avalanche is 0.2 mm/yr in the last 40 kyr. If we consider the central cluster as the oldest one (excepted for the northernmost scar for which only some discontinuous evidence of a deposit has been observed), and the absence of wave reworking of the deposit, then by summing up all the volumes for all the clusters we obtain a sediment yield of about $5.3 * 10^6$ t/kyr for the studied area (about 19 km^2; ca 277,650 t/kyr km^{-2}). This value, even if a rough one, can be considered as a first quantitative estimate of the erosion of the coastal scarp by large rock sliding/avalanching phenomena. In terms of erosion rate, we obtain an average value between 0.091 and 0.112 mm/yr. These values are in the same ranges of 0.01 and 0.08 mm/yr and 0.2 and 7 mm/yr presented by Keefer (1994) and Malamud et al. (2004), respectively, for earthquake induced landslides. This is by a third lower (0.307 mm/yr) than strongly tectonized and glaciated valleys that are predominantly eroded by rock-avalanche activity at the transition from the Central to the Patagonian Andes (Penna et al., 2015). This estimate could be extended, with all the due care, to the coastal scarp between Iquique and Arica to the north. In fact, this sector is characterized by the presence of the coastal plain, whereas to the north of Iquique, this is missing and the ocean directly erodes the toe of the coastal scarp, which could result in a more intense slope evolution, in terms of both frequency and size of the events. At present this value is under verification for such an area on the basis of a more detailed landslide inventory (see Crosta et al., 2014) directed to the study of both coastal and inland landslides.

As mentioned in the introduction, it is commonly observed that earthquake-induced landslides affect the upper part of the slopes, whereas rainfall induced ones preferentially occur at or affect the slope toe. The three clusters in the study area are all characterized by scars located in the upper slope sectors, affecting the rim of the coastal scarp. This suggests a dominant role in the triggering by large earthquakes and by local topographic amplification. Furthermore, a component associated with the relative orientation of the scarp with respect to the seismic source cannot be excluded. Even if no other evident rock avalanche is recognized close to these clusters, many other alcoves of similar shape and dimension are visible. These last have no associated deposit, possibly because of wave action when coastal plain was still submerged, and could suggest a very long history of successive failures and sediment delivery. Considering this, and some further observations in the area (Crosta et al., 2012, 2014), it is suggested that shallow crustal earthquakes could have been the most probable type of events capable of triggering such slope failures.

If seismic triggering is the most probable cause for these rock avalanches, it can be considered that after the initial large collapse, as discussed by Hermanns et al. (2006), some major sectors of the upper slope could have become unstable due to sudden mass release and related stress release in the underlying rocks to expose them to be triggered by subsequent smaller earthquakes or also by minor wet periods. This last possibility can be discarded due to the absence of erosion features that could be associated with running water. So, the recurrence of the events by seismic shaking should be evaluated with caution. A rough grouping of the datings obtained for the different rock-avalanche lobes results in 7 main events over a relatively long time span (60 + 7–10 kyr).

Regarding the observed mobility, these phenomena are less mobile than other similar events, when analyzed on the basis of the so called Heim's ratio, H/L and its relationship with volume. This reduced mobility could be the result of the extremely dry conditions existing at this site with respect to those typical of many rock avalanches observed worldwide and often associated with mountainous environments or with triggering by intense and prolonged rainfall.

From Fig. 13, it can be noted that the H/L versus volume relationship is good for the rock avalanches in the central cluster and along the same relationship is positioned the southern rock avalanche value. Some deviation is observed for the northern cluster where the LN3 lobes (LN3n, c, s) are slightly below the trend. This could be partially due to the different source area for these three events, being located just outside (S) the larger scar. When compared to the worldwide dataset for rock avalanches, it can be observed that the Iquique rock avalanches plot close to the upper limit of the dataset, thus suggesting a relatively low mobility with respect to other rock avalanches. This could be associated with some local environmental conditions controlling the material properties both for the rock avalanche and the underlying basal material. From another point of view, all the lobes present very similar aspect ratios, in particular in terms of length with respect to maximum width and to thickness, suggesting again a persistence of material and environmental properties during the entire history of the clusters.

Numerical modeling succeeds at describing the events, in terms of lobe geometry and thickness, by adopting a Bingham rheology, whereas frictional and Voellmy's rheologies always resulted in larger deposits, with incongruent thicknesses and deposit distributions. These results could be extremely useful for hazard zonation for rock avalanches occurring along the coastal scarp and plain.

10. Conclusions

The coastal area of northern Chile is characterized by an extremely dry climate and an extremely high seismicity. We studied an area just south to Iquique, characterized by a high concentration of rock avalanches with well-preserved deposits. Knowledge of their origin and triggering is fundamental from a geological and geomorphological point of view and for assessing the potential hazard and risk in the area. Dating of the three main clusters suggests that events span 60 ± 10 kyr in the central cluster, are younger by 20 kyr or more in the northern cluster, and are of a similar age range in the southern cluster. All rock avalanches certainly occurred when the coastal plain was already well above the sea level. Events are characterized by similar mobility even if separated in time. The triggering was probably the seismic activity and it was favored by the local orientation and geometry of the slope. The numerical modeling of rock avalanche runout succeeded at simulating the mass distribution when adopting a Bingham type rheology, providing a calibration useful for simulation of future events.

A sediment yield has been obtained for the area thanks to volume estimates and absolute dating. The computed values of erosion rate (0.091 to 0.112 mm/yr km^{-2}) are within the range presented in the literature for earthquake induced landslides. This can be a first quantitative estimate of the contribution of large landslide activity to the erosion of the coastal scarp in the area of northern Chile. This estimate is currently under testing by a more detailed landslide inventory for the entire area north of Iquique to Arica and it will be a subject of another contribution.

Supplementary data to this article can be found online at http://dx.doi.org/10.1016/j.geomorph.2016.11.024.

Acknowledgements

The research has been partially funded by the PRIN-MIUR 2010–2011 - 2010E89BPY_007 project and support by the International Centre of Geohazards to the NGU team. The suggestions by three anonymous reviewers helped at improving the manuscript. The authors wish to thank Adrian Harvey for the text supervision and advices.

References

Abele, G., 1974. Bergstürze in den Alpen: ihre Verbreitung, Morphologie und Folgeerscheinungen. Univ.-Verlag Wagner.

Adams, J., 1981. Earthquake-dammed lakes in New Zealand. Geology 9, 215–219.

Ambraseys, N., Bilham, R., 2012. The Sarez-Pamir earthquake and landslide of 18 February 1911. Seismol. Res. Lett. 83, 294–314.

Antinao, J.L., Gosse, J., 2009. Large rockslides in the Southern Central Andes of Chile (32–34.5°S): tectonic control and significance for Quaternary landscape evolution. Geomorphology 104, 117–133.

Baker, A., Allmendinger, R.W., Owen, L.A., Rech, J.A., 2013. Permanent deformation caused by subduction earthquakes in northern Chile. Nat. Geosci. 6, 492–496.

Balco, G., Stone, J.O., Lifton, N.A., Dunai, T.J., 2008. A complete and easily accessible means of calculating surface exposure ages or erosion rates from 10Be and 26Al measurements. Quat. Geochronol. 3, 174–195.

Beck, S.L., Ruff, L.J., 1989. Great earthquakes and subduction along the Peru trench. Phys. Earth Planet. Inter. 57, 199–224.

Bouchon, M., Schultz, C.A., Toksoz, M.N., 1996. Effect of three dimensional topography on seismic motion. J. Geophys. Res. 101, 835–846.

Chen, H., Lee, C.F., 2000. Numerical simulation of debris flows. Can. Geotech. J. 37, 146–160.

Crosta, G.B., Chen, H., Lee, C.F., 2004. Replay of the 1987 Val Pola Landslide, Italian Alps. Geomorphology 60, 127–146.

Crosta, G.B., Chen, H., Frattini, P., 2006. Forecasting hazard scenarios and implications for the evaluation of countermeasure efficiency for large debris avalanches. Eng. Geol. 83:236–253. http://dx.doi.org/10.1016/j.enggeo.2005.06.039.

Crosta, G., Hermanns, R.L., Valbuzzi, E., Dehls, J., Yugsi Molina, F.X., Sepúlveda, S.A., 2012. Slope instabilities along the Western Andean escarpment and the main canyons in Northern Chile. EGU General Assembly 2012, Vienna, Austria, 22–27 April 2012. Geophysical Research Abstracts 14 (EGU2012–11343).

Crosta, G.B., Hermanns, R.L., Frattini, P., Valbuzzi, E., 2014. Large slope instabilities in Northern Chile: inventory, characterization and possible triggerings. Proceedings of the 3rd World Landslide Forum, 2–6 June 2014, Bejing. Volume 3: Targeted Landslides, pp. 175–181.

Dai, F.C., Xu, C., Yao, X., Xu, L., Tu, X.B., Gong, Q.M., 2011. Spatial distribution of landslides triggered by the 2008 ms 8.0 Wenchuan earthquake, China. J. Asian Earth Sci. 40, 883–895.

Diercksen, J.K., 2012. Landslides caused by the 8/15/2007 Pisco, Peru (Mw = 7.9) earthquake: a case study. (Master thesis, MSc). University of Washington 176 pp.

Dunning, S.A., Mitchell, W.A., Rosser, N.J., Petley, D.N., 2007. The Hattian Bala rock avalanche and associated landslides triggered by the Kashmir Earthquake of 8 October 2005. Eng. Geol. 93, 130–144.

Eisbacher, G.H., Clague, J.J., 1984. Destructive mass movements in High Mountains: hazard and management. Geol. Surv. Can. Pap. 84–16, 230.

Evans, S.G., Roberts, N.J., Ischuk, A., Delaney, K.B., Morozova, G.S., Tutubalina, O., 2009a. Landslides triggered by the 1949 Khait earthquake, Tajikistan, and associated loss of life. Eng. Geol. 109, 195–212.

Evans, S.G., Bishop, N.F., Fidel Smoll, L., Valderrama Murillo, P., Delaney, K.B., Oliver-Smith, A., 2009b. A re-examination of the mechanism and human impact of catastrophic mass flows originating on Nevado Huascarán, cordillera Blanca, Peru in 1962 and 1970. Eng. Geol. 108, 96–118.

Fredlund, D.G., Krahn, J., 1977. Comparison of slope stability methods of analysis. Can. Geotech. J. 14:429–439. http://dx.doi.org/10.1139/t77–045.

Gosse, J.C., Phillips, F.M., 2001. Terrestrial in situ cosmogenic nuclides; theory and application. Quat. Sci. Rev. 20, 1475–1560.

Hadley, J.B., 1964. Landslides and related phenomena accompanying the Hebgen Lake Earthquake of August 17, 1959. US Government Printing Office (pp. 435–138).

Hartley, A., Howell, J., Mather, A.E., Chong, G., 2001. A possible Plio-Pleistocene tsunami deposit Hornitos, northern Chile. Rev. Geol. Chile 28, 117–125.

Heim, A., 1932. Bergsturz und Menschenleben. Beiblatt zur Vierteljahresschrift der Naturforschenden Gesellschaft in Zürich, Zürich.

Heim, A., 1949. Observaciones geológicas en la región del terremoto de Ancash de noviembre de 1946. Soc. Geol. Perú 25, 2–21.

Hermanns, R.L., Niedermann, S., 2011. Late Pleistocene–Early Holocene paleoseismicity deduced from lake sediment deformation and coeval landsliding in the Calchaquíes valleys, NW Argentina. In: Audemard, F.A., Michetti, A., McCalpin, J.P. (Eds.), Geological Criteria for Evaluating Seismicity Revisited: Forty Years of Paleoseismic Investigations and the Natural Record of Past Earthquakes. Geological Society of America, Boulder, Special Paper 479, pp. 181–194.

Hermanns, R.L., Trauth, M.H., Niedermann, S., McWilliams, M., Strecker, M.R., 2000. Tephrochronologic constraints on temporal distribution of large landslides in NW-Argentina. J. Geol. 108, 35–52.

Hermanns, R.L., Niedermann, S., Villanueva Garcia, A., Sosa Gomez, J., Strecker, M.R., 2001. Neotectonics and catastrophic failure of mountain fronts in the southern intra-Andean Puna plateau, Argentina. Geology 29, 619–623.

Hermanns, R.L., Niedermann, S., Ivy-Ochs, S., Kubik, P.W., 2004. Rock avalanching into a landslide-dammed lake causing multiple dam failure in Las Conchas valley (NW Argentina) - evidence from surface exposure dating and stratigraphic analyses. Landslides 1, 113–122.

Hermanns, R.L., Blikra, L.H., Naumann, M., Nilsen, B., Panthi, K.K., Stromeyer, D., Longva, O., 2006. Examples of multiple rock-slope collapses from Köfels (Ötz valley, Austria) and western Norway. Eng. Geol. 83, 94–108.

Hermanns, R.L., Fauque, L., Fidel Small, L., Welkner, D., Folguera, A., Cazas, A., Nuñez, H., 2008. Overview of catastrophic mega-rockslides in the Andes of Argentina, Bolivia, Chile, Ecuador and Peru. The First Landslide World Forum, Tokyo, pp. 255–258.

Hermanns, R.L., Folguera, A., Penna, I.M., Fauque, L., 2011. Landslide dams in the Argentine Andes, relation between dam - and valley morphology, climate and long term stability. In: Evans, S.G., Hermanns, R.L., Scarascia Mugnozza, G., Strom, A. (Eds.), Natural and Artificial Rockslide DamsLecture Notes in Earth Sciences. Springer, Berlin, pp. 147–176.

Hermanns, R.L., Fauqué, L., Wilson, C.G., 2014. ^{36}Cl terrestrial cosmogenic nuclide dating suggests Late Pleistocene to Early Holocene mass movements on the south face of Aconcagua mountain and in the Las Cuevas–Horcones valleys. Central Andes, Argentina: Geological Society London, Special Publications 399, pp. 345–368.

Hungr, O., McDougall, S., 2009. Two numerical models for landslide dynamic analysis. Comput. Geosci. 35, 978–992.

Hungr, O., Salgado, F.M., Byrne, P.M., 1989. Evaluation of a three-dimensional method of slope stability analysis. Can. Geotech. J. 26, 679–686.

Ischuk, A.R., 2011. Usoi rockslide dam and lake Sarez, Pamir mountains, Tajikistan. In: Evans, S.G., Hermanns, R.L., Scarascia Mugnozza, G., Strom, A. (Eds.), Natural and Artificial Rockslide DamsLecture Notes in Earth Sciences. Springer, Berlin, Heidelberg, pp. 423–440.

Ivy-Ochs, S., Poschinger, A.v., Synal, H.A., Maisch, M., 2009. Surface exposure dating of the Flims landslide, Graubünden, Switzerland. Geomorphology 1003, 104–112.

Jibson, R.W., 2009. Using landslides for paleoseismic analysis. In: McCalpin, J.P. (Ed.), Paleoseismology. Academic Press, Burlington, pp. 565–601.

Jibson, R.W., Harp, E.L., Schulz, W., Keefer, D.K., 2006. Large rock avalanches triggered by the M 7.9 Denali fault, Alaska, earthquake of 3 November 2002. Eng. Geol. 83, 144–160.

Kampherm, T.S., 2009. Landslides triggered by the 1946 Ancash earthquake (Peru) and geologic controls on the mechanisms of initial rock slope failure. (Master thesis). waterloo University, Ontario, Canada, p. 126.

Keefer, D.K., 1984a. Landslides caused by earthquakes. Geol. Soc. Am. Bull. 95, 406–421.

Keefer, D.K., 1984b. Rock avalanches caused by earthquakes: source characteristics. Science 223, 1288–1290.

Keefer, D.K., 1994. The importance of earthquake-induced landslides to long-term slope erosion and slope-failure hazards in seismically active regions. Geomorphology 10, 265–284.

Keefer, D.K., Moseley, M.E., 2004. Southern Peru desert shattered by the great 2001 earthquake: implications for paleoseismic and paleo-El Niño southern oscillation records. Proc. Natl. Acad. Sci. U. S. A. 101, 10878–10883.

Kojan, E., Hutchinson, J.N., 1978. Mayunmarca rockslide and debris flow, Peru. In: Voight, B. (Ed.), Rockslides and Avalanches; 1, Natural Phenomena. Elsevier Scientific Publishing Company, Amsterdam, pp. 315–361.

Lal, D., 1991. Cosmic ray labeling of erosion surfaces; in situ nuclide production rates and erosion models. Earth Planet. Sci. Lett. 104, 424–439.

Lomnitz, C., 2004. Major earthquakes of Chile: a historical survey, 1535–1960. Seismol. Res. Lett. 75, 368–378.

Malamud, B.D., Turcotte, D.L., Guzzetti, F., Reichenbach, P., 2004. Landslides, earthquakes, and erosion. Earth Planet. Sci. Lett. 229, 45–59.

Mather, A.E., Hartley, A.J., Griffiths, J.S., 2014. The giant landslides of northern Chile: tectonic and climate interactions on a classic convergent plate margin. Earth Planet. Sci. Lett. 388, 249–256.

Meunier, P., Hovius, N., Haines, A.J., 2007. Regional patterns of earthquake-triggered landslides and their relation to ground motion. Geophys. Res. Lett. 34, L20408. http://dx.doi.org/10.1029/2007GL031337.

Meunier, P., Hovius, N., Haines, J.A., 2008. Topographic site effects and the location of earthquake induced landslides. Earth Planet. Sci. Lett. 275, 221–232.

Miller, D.J., 1960. Giant waves in Lituya Bay, Alaska. U.S·Geological Survey Professional Paper 354C, pp. 51–86.

Montandon, F., 1933. Chronologie des grands eboulements alpins du debut de l'ere chretienne a nos jours. Matériaux Pouri l'étude Des calamités Societe de Geographie Geneve 32, pp. 271–340.

Moreiras, S.M., Hermanns, R.L., Fauqué, L., 2015. Cosmogenic dating of rock avalanches constraining Quaternary stratigraphy and regional neotectonics in the Argentine Central Andes (32° S). Quat. Sci. Rev. 112, 45–58.

Novoa, A.T., 1970. Carta Geológica de Chile: Cuadrángulos Iquique y Caleta Molle: Provincia de Tarapacá. Instituto de Investigaciones Geológicas(Chile). Carta Geológica, pp. 21–22.

Owen, L.A., Kamp, U., Khattak, G.A., Harp, E.L., Keefer, D.K., Bauer, M.A., 2008. Landslides triggered by the 8 October 2005 Kashmir earthquake. Geomorphology 94, 1–9.

Paskoff, R., 1978. Sur l'évolution geomorphologique du grand escarpement côtier du désert Chilien. Geog. Phys. Quat. 32, 351–360.

Penna, I.M., Hermanns, R.L., Folguera, A., Niedermann, S., 2011. Multiple slope failures associated with neotectonic activity in the southern Central Andes (37°–37°30′S). Patagonia, Argentina. Geol. Soc. Am. Bull. 123, 1880–1895.

Penna, I.M., Hermanns, R.L., Daicz, S., Suriano, J., Tedesco, A.M., 2015. Effects of tectonic deformation and landslides in the erosion of a mountain plateau in the transitional zone between the central and Patagonian Andes. Am. J. Sci. 315, 257–274.

Pinto, L., Herail, G., Sepúlveda, S., Krop, P., 2008. A neogene giant landslide in Tarapaca, northern Chile: a signal of instability of the westernmost Altiplano and paleoseismicity effects. Geomorphology 102, 532–541.

Plafker, G., Ericksen, G.E., 1978. Nevados Huascaran avalanches, Peru. In: Voight, B. (Ed.), Rockslides and Avalanches. Elsevier, Amsterdam, pp. 277–314.

Post, A., 1967. Effects of the March 1964 Alaska earthquake on glaciers. U.S. Geological Survey Professional Paper 544–D:p. 54 (http://pubs.usgs.gov/pp/0544d/).

Quezada, J., Bataille, K., Gonzàlez, G., 2006. The effect of subduction earthquakes on the coastal configuration of Northern Chile. 6th International Symposium on Andean Geodynamics (ISAG 2005, Barcelona), Extended Abstracts, 578·581.

Regard, V., Saillard, M., Martinod, J., Audin, L., Carretier, S., Pedoja, K., Riquelme, R., Paredes, P., Hérail, G., 2010. Renewed uplift of the Central Andes Forearc revealed by coastal evolution during the Quaternary. Earth Planet. Sci. Lett. 297:199–210. http://dx.doi.org/10.1016/j.epsl.2010.06.020.

Rodríguez, C.E., Bommer, J.J., Chandler, R.J., 1999. Earthquake-induced landslides: 1980–1997. Soil Dyn. Earthq. Eng. 18, 325–346.

Savage, S.B., Hutter, K., 1989. The motion of a finite mass of granular material down a rough incline. J. Fluid Mech. 199, 177–215.
Scheidegger, A.E., 1973. On the prediction of the reach and velocity of catastrophic landslides. Rock Mech. 5, 231–236.
Sepulveda, S., Serey, A., Lara, M., Pavez, A., Rebolledo, S., 2010. Landslides induced by the April 2007 Aysén fjord earthquake, Chilean Patagonia. Landslides 7, 483–492.
Shreve, R.L., 1966. Sherman landslide, Alaska. Science 154, 1639–1643.
Sosio, R., Crosta, G., Chen, J., Hungr, O., 2012. Modelling rock avalanche propagation onto glaciers. Quat. Sci. Rev. 47, 23–40.
Stone, J.O., 2000. Air pressure and cosmogenic isotope production. J. Geophys. Res. 105, 23753–23759.
Strasser, M., Schlunegger, F., 2005. Erosional processes. Topographic length scales and geomorphic evolution in arid climatic environments: the Lluta collapse, northern Chile. Int. J. Earth Sci. 94, 433–446.
Strom, A., 2015. Clustering of large bedrock landslides and recurrent slope failure: implications for land seismic hazard assessment of the Tien Shan-Djungaria region. Int. J. Geohazards Environ. 1 (3), 110–121.
Ui, T., 1983. Volcanic dry avalanche deposits—identification and comparison with nonvolcanic debris stream deposits. J. Volcanol. Geotherm. Res. 18, 135–150.
Utili, S., Crosta, G.B., 2011. Modelling the evolution of natural cliffs subject to weathering: I. Limit analysis approach. J. Geophys. Res. 116, F01017. http://dx.doi.org/10.1029/2009JF001557.
Weischet, W., 1960. Die geographischen Auswirkungen des erdbebens vom 22. mai 1960 im kleinen Süden Chiles. Erdkunde 14, 273–288.
Welkner, D., Eberhardt, E., Hermanns, R.L., 2010. Hazard investigation of the Portillo Rock Avalanche site, central Andes, Chile, using an integrated field mapping and numerical modelling approach. Eng. Geol. 114, 278–297.
Wörner, G., Uhlig, D., Kohler, I., Seyfried, H., 2002. Evolution of the west Andean escarpment at 18°S (N. Chile) during the last 25 ma: uplift, erosion and collapse through time. Tectonophysics 345, 183–198.
Wu, S., Wang, T., Shi, L., Sun, P., Shi, J., Li, B., Wang, H., 2010. Study on catastrophic landslides triggered by 2008 great Wenchuan earthquake, Sichuan, China. J. Eng. Geol. 18, 145–159.
Yin, Y., Zheng, W., Li, X., Sun, P., Li, B., 2011. Catastrophic landslides associated with the M8. 0 Wenchuan earthquake. Bull. Eng. Geol. Environ. 70, 15–32.
Yugsi Molina, F.X., Hermanns, R.L., Dehls, J., Crosta, G.B., Sosio, R., Sepúlveda, S., 2012a. Large rock avalanches in Northern Chile, an integrated analysis towards regional hazard assessment. Actas XIII Congreso Geológico Chileno, pp. 1027–1029.
Yugsi Molina, F.X., Hermanns, R.L., Crosta, G.B., Dehls, J., Sosio, R., Sepúlveda, S.A., 2012b. Geomorphological analysis, monitoring and modeling of large rock avalanches in northern Chile (Iquique area) for regional hazard assessment. EGU General Assembly 2012, Held 22–27 April 2012, Vienna, Austria. Copernicus, p. 8925 (2012EGUGA.14.8925Y).
Zavala, B., Hermanns, R.L., Valderrama, P., Costa, C., Rosado, M., 2009. Procesos geológicos e inestabilidad macrosísmica INQUA del sismo de Pisco del 15/08/2007, Perú. Rev. Asoc. Geol. Argent. 65, 760–779.